

How two-dimensional are planet–disc interactions? I. Locally isothermal discs

Amelia J. Cordwell ¹*, Alexandros Ziampras^{2,3,4}, Joshua J. Brown¹, and Roman R. Rafikov^{1,5}

¹Department of Applied Mathematics and Theoretical Physics, University of Cambridge, Wilberforce Road, Cambridge CB3 0WA, UK

²Ludwig-Maximilians-Universität München, Universitäts-Sternwarte, Scheinerstr. 1, 81679 München, Germany

³Astronomy Unit, Dept. of Physics and Astronomy, Queen Mary University of London, London E1 4NS, UK

⁴Max Planck Institute for Astronomy, Königstuhl 17, 69117 Heidelberg, Germany

⁵Institute for Advanced Study, Einstein Drive, Princeton, NJ 08540, USA

arXiv:2509.04282v2 [astro-ph.EP] 3 Oct 2025

Accepted XXX. Received YYY; in original form ZZZ

ABSTRACT

Planet–disc interactions, despite being fundamentally three-dimensional, are often studied in the two-dimensional ‘thin-disk’ approximation. The overall morphology of planet–disc interactions has been shown to be similar in both 2D and 3D simulations, however, the ability of a 2D simulation to quantitatively match 3D results depends strongly on how the potential of the planet is handled. Typically, the 2D planetary potential is smoothed out using some ‘smoothing length’, a free parameter, for which different values have been proposed, depending on the particular aspect of the interaction of interest. In this paper, we re-derive 2D Navier–Stokes in detail for planet–disc interactions to find better ways to represent the 2D gravitational force. We perform a large suite of 2D and 3D simulations to test these force prescriptions. We identify the parts of the interaction that are fundamentally 3D, and test how well our new force prescriptions, as well as traditional smoothed potentials, are able to match 3D simulations. Overall, we find that the optimal way to represent the planetary potential is the ‘Bessel-type potential’, but that even in this case 2D simulations are unable to reproduce the correct scaling of the total torque with background gradients, and are at best able to match the one-sided Lindblad torque and gap widths to level of 10 per cent. We find that analysis of observed gap structures based on standard 2D simulations may systematically underestimate planetary masses by a factor of two, and discuss the impacts of 3D effects on observations of velocity kinks.

Key words: planet–disc interactions – hydrodynamics – protoplanetary discs – planets and satellites: formation

1 INTRODUCTION

Planets have significant and complex interactions with their natal environment of protoplanetary discs including accretion, migration and gap formation (for a recent review, see [Paardekooper et al. 2022](#)). They are one of the causes for rings and gaps seen in dust emission in protoplanetary discs ([Andrews 2020](#)), and the waves excited by planet–disc interactions can be observed in their kinematic signatures (e.g. [Pinte et al. 2023](#); [Teague et al. 2025](#)).

While the planet–disc interaction is inherently a three-dimensional (3D) process, a two-dimensional (2D) approximation is often used to simplify the complex interaction in both numerical and analytical studies. In the 2D approximation one operates with the 2D fluid equations formulated for the vertically averaged velocities in the plane of the disc (ignoring the velocity perpendicular to the disc plane) and the surface density of the disc Σ (instead of the volumetric gas density ρ). Formal derivation of such 2D equations from their full 3D analogues in a disc without a planet has been provided in the past assuming the disc to be in a vertical hydrostatic equilibrium ([Hunter 1972](#); [Churilov & Shukhman 1981](#); [Goldreich et al. 1986](#); [Ostriker et al. 1992](#); [Fridman & Khoruzhii 1996](#)). Such a projection of the

3D equations onto two dimensions typically results in a non-trivial modification of the pressure-density relation.

In the planet-disc context the 2D-3D correspondence has been justified in part because the majority of the angular momentum, arising from interactions with planets on non-inclined orbits, is carried in ‘2D waves’, i.e. waves with no vertical velocity ([Takeuchi & Miyama 1998](#)). In addition, the width of the horseshoe co-orbital region is near invariant with altitude above the midplane in vertically isothermal discs ([Fung et al. 2015](#); [Masset & Benítez-Llambay 2016](#)). Moreover, gaps carved by planets are qualitatively similar in 2D and 3D simulations ([Fung & Chiang 2016](#)).

When transitioning from 3D to 2D in the planet-disc case, one needs to worry about the vertical averaging of the gravitational force exerted by the planet on the disc. In numerical work, this averaging is often implemented approximately, by resorting to some form of the smoothed gravitational potential. Smoothing over some characteristic length r_s was introduced initially (e.g. [Takeuchi & Miyama 1998](#); [Kley 1999](#); [D’Angelo et al. 2002](#)) to deal with the numerical singularity of the standard Keplerian gravitational potential, $\Phi_K \equiv -GM_p/|\mathbf{R} - \mathbf{R}_p|$ at $\mathbf{R} = \mathbf{R}_p$, but later its use was extended to mimic the effect of vertical averaging of the planetary gravity in 2D simulations. The specific form of the smoothed potential varies, in particular [Dong et al. \(2011a\)](#) proposed several forms of the potential which differ in terms of the rate at which they converge to Φ_K far

* E-mail: ajc356@cam.ac.uk

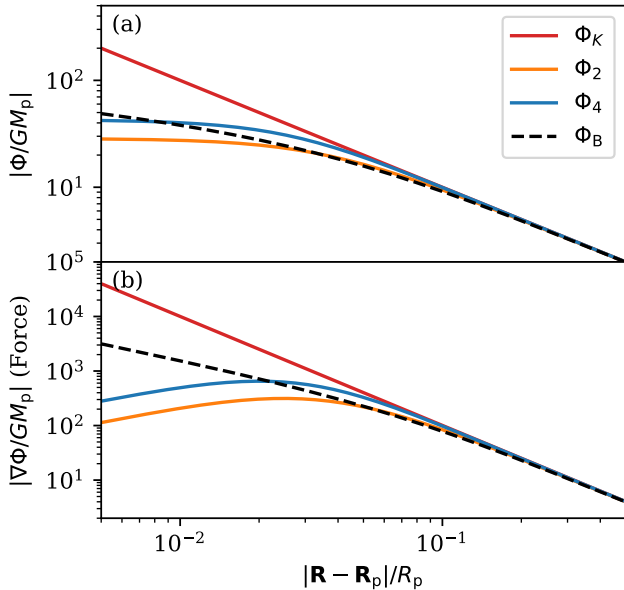


Figure 1. Gravitational potential (a) and acceleration (b) for the different types of planetary potential considered in this paper, shown in units $GM_p = 1$. Φ_K is the standard Keplerian potential, Φ_2 (Equation 1) and Φ_4 (Equation 26) are the second and fourth order smoothed potentials using a smoothing length of $r_s = bH$ with $b = 0.7$. Φ_B is the Bessel-type potential (Equation 25). All potentials were calculated for a reference disc with a constant scale height of $H = 0.05R_p$. All potentials converge to Φ_K far from the planet, however near the planet there are significant differences, especially, in acceleration.

from the planet. In numerical applications, the most often used is the second order smoothed potential,

$$\Phi_2 \equiv -\frac{GM_p}{\sqrt{|\mathbf{R} - \mathbf{R}_p|^2 + r_s^2}}, \quad (1)$$

although other forms (e.g. Φ_4 , see Cimerman & Rafikov 2021, and equation (26) and Figure 1) are occasionally used as well. The smoothing length r_s is often written as a fraction of the local scale height $r_s = bH$.

The choice of r_s affects various aspects of the disc-planet coupling, and its value is usually selected based on the requirement that the 2D results match a particular metric in a full 3D calculation. For example, using the standard Keplerian gravitational potential with minimal softening only to avoid numerical singularities in a 2D simulation leads to a one-sided torque excited by the planet that is twice as large as that in an equivalent 3D simulation (Miyoshi et al. 1999). To make the value (and overall structure) of the excited torque in 2D simulations similar to 3D, Müller et al. (2012) suggested using $b = 0.7$ with the Φ_2 potential, although other analyses using the same metric (e.g. Masset 2002; Fung et al. 2015) found slightly different optimal smoothing lengths.

If instead of one-sided torque one uses as a metric the total (or migration) torque applied to the planet, then an optimal value of $b = 0.4$ may be more appropriate (Paardekooper et al. 2010, 2011). However, Tanaka & Okada (2024) showed that no value of b in Φ_2 is capable of reproducing the scaling of the migration torque obtained in 3D with the background gradients of temperature and surface density in the disc.

Yet another metric of 2D-3D correspondence can be formulated by considering the shape of the structures forming in the disc around

the planet. For example, Fung & Chiang (2016) found that using $b = 0.5$ provides an optimal match to the shape of the gaps carved by the planet in a disc.

Smoothed potentials different from Φ_2 or Φ_4 are also possible. Recently, Brown & Ogilvie (2024) suggested that yet another form of the potential (Φ_{B,H_p}) would more effectively capture 3D physics in 2D simulations (we show the shape of their suggested potential in Figure 1). However, their analytical work was carried out in the shearing box approximation, and as such it did not include the effect of background gradients in the disc; their prescription was also not tested in simulations.

In this paper, we re-assess the correspondence between the 2D and 3D calculations of disc-planet coupling focusing on discs with a particularly simple thermodynamics. Namely, we consider locally isothermal discs, that is discs with no vertical temperature gradient and a simple equation of state (EoS) in the form

$$P = c_s^2 \rho, \quad (2)$$

where P is pressure and c_s is the sound speed, which can be spatially varying. A specific question we aim to address is what prescription for the planetary gravitational potential ensures the closest correspondence between 2D and 3D results?

Starting from the 3D fluid equations, we re-derive the equations of motion for an isothermal 2D disc and use these to define four different physically motivated forms of the gravitational force due to a planet. Then, we test both these forms and traditional smoothed potentials in 2D and compare results against 3D hydrodynamic simulations. In doing this we examine the impact of the force prescriptions on the torque excitation and angular momentum deposition, as well as on the structures that form in the disc.

The plan of this paper is as follows. In Section 2, we show one method to define a 2D disc from the 3D Navier–Stokes equations and then after defining our specific disc model in Section 3, describe all of the ways we represent the 2D planetary gravitational force in our simulations in Section 4. In Section 5, we describe our numerical methods and the metrics we use with which to analyse our simulations. In Section 6, we present our results. We first describe which parts of the 3D simulations are unable to be represented in 2D, before comparing 2D and 3D simulations directly. In this section, we also calculate optimal smoothing lengths for traditional smoothed potentials across a range of metrics. In Section 7, we discuss the implications of our work before summarizing our key findings in Section 8. We include additional derivations and numerical tests in the Appendix.

This paper only considers locally (and vertically) isothermal discs. The second work in this series (Ziampras et al. 2025) discusses the impacts that more realistic thermodynamics have on the convergence between gap structures in 2D and 3D simulations.

2 REDUCTION FROM 3D TO 2D

In this section, we perform a direct vertical averaging of the fluid equations to motivate the form of the standard 2D fluid equations in disc-planet coupling. We will use $\mathbf{v}(R, \phi, z)$ to denote 3D vector velocity, and $\mathbf{u}(R, \phi)$ to denote the 2D velocity, which we define as

$$\mathbf{u}(R, \phi) \equiv \frac{1}{\Sigma} \int_{-\infty}^{\infty} \rho \mathbf{v} dz, \text{ where} \quad (3)$$

$$\Sigma(R, \phi) \equiv \int_{-\infty}^{\infty} \rho dz \quad (4)$$

is the surface density. This definition of \mathbf{u} is momentum-based as density weighting is adopted. We also define velocity deviation from its vertical average

$$\delta\mathbf{v}(R, \phi, z) \equiv \mathbf{v}(R, \phi, z) - \mathbf{u}(R, \phi). \quad (5)$$

Clearly, $\int_{-\infty}^{\infty} \rho \delta\mathbf{v} dz = 0$.

In 3D fluid equations — Navier-Stokes and continuity — read

$$\rho \left(\frac{\partial \mathbf{v}}{\partial t} + (\mathbf{v} \cdot \nabla) \mathbf{v} \right) = -\nabla P - \rho \nabla \Phi, \quad (6)$$

$$\frac{\partial \rho}{\partial t} + \nabla \cdot (\rho \mathbf{v}) = 0, \quad (7)$$

where P is the 3D pressure and Φ is the full gravitational potential. Multiplying the continuity equation by \mathbf{v} and adding the result to (6), one obtains

$$\frac{\partial(\rho\mathbf{v})}{\partial t} + (\rho\mathbf{v} \cdot \nabla) \mathbf{v} + \mathbf{v} (\nabla \cdot (\rho\mathbf{v})) = -\nabla P - \rho \nabla \Phi. \quad (8)$$

Next, we integrate this equation over z from $-\infty$ to ∞ . The first term on the left becomes $\partial(\Sigma\mathbf{u})/\partial t$ without any additional assumptions. When manipulating the next two terms we separate spatial derivatives in the direction parallel to the disk midplane (∇_{\parallel}) and normal to it (i.e. $\partial/\partial z$). Then

$$\begin{aligned} \int_{-\infty}^{\infty} dz [(\rho\mathbf{v} \cdot \nabla) \mathbf{v} + \mathbf{v} (\nabla \cdot (\rho\mathbf{v}))] = \\ \int_{-\infty}^{\infty} dz \left[(\rho\mathbf{v}_{\parallel} \cdot \nabla_{\parallel}) \mathbf{v} + \mathbf{v} (\nabla_{\parallel} \cdot (\rho\mathbf{v}_{\parallel})) + \rho v_z \frac{\partial \mathbf{v}}{\partial z} + \mathbf{v} \frac{\partial(\rho v_z)}{\partial z} \right]. \end{aligned} \quad (9)$$

Last two terms combine to $\partial(\rho v_z \mathbf{v})/\partial z$ and integrate to zero, provided that $\rho \rightarrow 0$ as $|z| \rightarrow \infty$.

In the remaining two terms we substitute $\mathbf{v} = \mathbf{u} + \delta\mathbf{v}$:

$$\begin{aligned} \int_{-\infty}^{\infty} dz \left[(\rho\mathbf{v}_{\parallel} \cdot \nabla_{\parallel}) \mathbf{u} + \mathbf{u} (\nabla_{\parallel} \cdot (\rho\mathbf{v}_{\parallel})) + (\rho\mathbf{v}_{\parallel} \cdot \nabla_{\parallel}) \delta\mathbf{v} \right. \\ \left. + \delta\mathbf{v} (\nabla_{\parallel} \cdot (\rho\mathbf{v}_{\parallel})) \right] = (\Sigma\mathbf{u} \cdot \nabla) \mathbf{u} + \mathbf{u} (\nabla \cdot (\Sigma\mathbf{u})) + \Delta, \end{aligned} \quad (10)$$

where in the first two terms (obtained without making any approximations) we dropped the \parallel subscript, assuming now $\mathbf{u} = (u_R, u_{\phi})$ to be the usual 2D in-plane velocity (from now on we will not be interested in u_z) and $\nabla = \nabla_{\parallel}$ to denote gradients within the disc plane. Also, along the disc plane the (vector) remainder term is

$$\Delta = \int_{-\infty}^{\infty} dz \left[(\rho\mathbf{v}_{\parallel} \cdot \nabla_{\parallel}) \delta\mathbf{v}_{\parallel} + \delta\mathbf{v}_{\parallel} (\nabla_{\parallel} \cdot (\rho\mathbf{v}_{\parallel})) \right] \quad (11)$$

$$= \nabla \cdot \hat{P}_{\text{dyn}}, \quad \text{where} \quad \hat{P}_{\text{dyn}} = \int_{-\infty}^{\infty} (\rho \delta\mathbf{v}_{\parallel} (\delta\mathbf{v}_{\parallel})^{\top}) dz. \quad (12)$$

To obtain (12) we substituted $\mathbf{v}_{\parallel} = \mathbf{u} + \delta\mathbf{v}_{\parallel}$ and carried out integration over z where appropriate. This term depends on the deviation of the 3D velocity along the disc plane $\mathbf{v}_{\parallel} = (v_R, v_{\phi})$ from its vertically averaged counterpart \mathbf{u} . One can see that Δ is the divergence of the 'dynamic stress tensor' \hat{P}_{dyn} , which arises because of the vertical variation of fluid velocities in the disc.

Substituting these results into the vertically integrated equation (8) for the in-plane velocity components, we find

$$\frac{\partial(\Sigma\mathbf{u})}{\partial t} + (\Sigma\mathbf{u} \cdot \nabla) \mathbf{u} + \mathbf{u} (\nabla \cdot (\Sigma\mathbf{u})) + \Delta = -\nabla P_{2D} + \Sigma \mathbf{a}, \quad (13)$$

where $P_{2D} \equiv \int_{-\infty}^{\infty} P dz$ is the '2D' pressure and

$$\mathbf{a} = -\frac{1}{\Sigma} \int_{-\infty}^{\infty} \rho (\nabla_{\parallel} \Phi) dz \quad (14)$$

is the '2D gravitational acceleration'.

Next, we integrate the continuity equation (7) over z . Manipulating its terms analogous to the equations (9), (10), we obtain, without any assumptions, the 2D version of the continuity equation

$$\frac{\partial \Sigma}{\partial t} + \nabla \cdot (\Sigma \mathbf{u}) = 0, \quad (15)$$

where again $\nabla = \nabla_{\parallel}$ in 2D.

Multiplying (15) by \mathbf{u} and subtracting it from (13), we can re-write the equation of motion (13) in the following form:

$$\Sigma \left[\frac{\partial \mathbf{u}}{\partial t} + (\mathbf{u} \cdot \nabla) \mathbf{u} \right] + \Delta = -\nabla P_{2D} + \Sigma \mathbf{a}. \quad (16)$$

This equation would look like the standard 2D Navier-Stokes equation if one could neglect Δ compared to all other terms. An alternative approximate procedure for deriving the 2D disc equations via a projection of the linearized Navier-Stokes equations onto vertical modes is demonstrated in Appendix A.

This derivation demonstrates that the reduction of the fluid equations (6), (7) from 3D to the 'standard' 2D fluid equations is not perfect in general. In other words, if one obtains ρ and \mathbf{v} from a 3D simulation and computes Σ and \mathbf{u} from this data using definitions (3), (4), the result would differ from the Σ and \mathbf{u} computed using 2D fluid equations with some assumptions regarding P_{2D} and \mathbf{a} . There are three reasons for that.

First, Δ need not be small and may provide a non-negligible contribution in the equation (16). Its amplitude needs to be assessed explicitly in every problem under consideration. However, in some cases, when e.g. \mathbf{v}_{\parallel} varies with z weakly near the disc midplane where ρ is high (i.e. motion is 'quasi-2D'), one would expect $|\delta\mathbf{v}_{\parallel}| \ll |\mathbf{v}_{\parallel}|$ and correspondingly, Δ being subdominant as it is quadratic in $\delta\mathbf{v}_{\parallel}$. Also, one expects $|\Delta| \ll |\nabla P_{2D}|$ when $|\delta\mathbf{v}_{\parallel}| \ll c_s$, which should be easy to satisfy.

Second, P_{2D} is not necessarily a simple (and similarly looking) function of Σ as P is a function of ρ in 3D. If $P \propto \rho^{\gamma}$ with $\gamma \neq 1$, then the relation between P_{2D} and Σ will involve factors depending on the vertical profile of ρ , which could also be time-dependent. Even when the vertical hydrostatic equilibrium is assumed, the polytropic index of $P_{2D}(\Sigma)$ dependence has been shown to differ from γ in both self-gravitating (Hunter 1972; Fridman & Khoruzhii 1996) and non-self-gravitating discs (Churilov & Shukhman 1981; Goldreich et al. 1986; Ostriker et al. 1992). However, in a disc with an isothermal EoS (Equation 2) the 2D pressure relation is also simple¹: $P_{2D} = c_s^2 \Sigma$, even if c_s is non-uniform. This is the situation we consider in this paper.

Third, in 2D one generally writes \mathbf{a} as a gradient of some '2D potential', $\mathbf{a} = -\nabla \Phi_{2D}$. Looking at equation (14), this is only possible if ρ and Σ were independent of in-plane coordinates (like in a shearing sheet approximation), as in this case \mathbf{a} could be written as

$$\mathbf{a} = -\nabla_{\parallel} \left(\frac{1}{\Sigma} \int_{-\infty}^{\infty} \rho \Phi dz \right). \quad (17)$$

However, even in this case in an evolving disc with ρ changing in time, the effective 2D potential would end up being explicitly time-dependent. And in a more realistic situation where ρ and Σ vary in the disc plane, writing \mathbf{a} as a gradient of some Φ_{2D} would not even be possible. In the next section we describe several possible models for \mathbf{a} in 2D, which we test later (see Section 6) numerically in an attempt to optimize the 2D-3D correspondence.

¹ Brown & Ogilvie (2024) found a simple relation also when considering a vertically isothermal density structure but non-isothermal pressure response to perturbations.

3 MODEL SETUP

Next we describe the physical setup of the planet-disc problem that we focus on. We consider a 3D gaseous disc, initially in hydrostatic equilibrium, orbiting around a star of mass M_\star . The disc is described in cylindrical co-ordinates $\{R, \phi, z\}$, with the mid-plane of the disc located at $z = 0$. The disc is inviscid and non-self-gravitating. This disc is perturbed by an embedded planet, with mass M_p , on a zero-inclination and circular orbit with semi-major axis R_p .

To describe the thermodynamics of the disc, we use the locally isothermal equation of state (2). The disc is also vertically isothermal, with its temperature depending only on R . In this case, prior to the introduction of a planet, the initial vertical density distribution is

$$\rho_0 = \frac{\Sigma_0}{\sqrt{2\pi}H} \exp\left(\frac{-z^2}{2H^2}\right), \quad (18)$$

where $\Sigma_0 \equiv \int_{-\infty}^{\infty} \rho_0 dz$ is the initial surface density, the scale height is $H \equiv c_s/\Omega_K$, Ω_K is the Keplerian angular frequency, and c_s is the isothermal sound speed.

The initial axisymmetric surface density, temperature and sound speed profiles of the disc are

$$\Sigma_0 = \Sigma_p \left(\frac{R}{R_p}\right)^{-p}, \quad T = T_p \left(\frac{R}{R_p}\right)^{-q}, \quad c_s = c_{s,p} \left(\frac{R}{R_p}\right)^{-q/2}, \quad (19)$$

where the subscript ‘p’ indicates a value defined at $R = R_p$, and q and p are constant power law indices.

In a globally isothermal, inviscid disc with no explicit dissipation the planet-driven wake deposits angular momentum only after it shocks. For $q \neq 0$, the wave can gain or lose angular momentum from the background disc as it propagates through the regions of higher or lower temperature it (Miranda & Rafikov 2019a). However, for the (reasonably high) planetary mass we consider in this paper this effect is negligible in comparison to shock-driven deposition and will be ignored.

4 GRAVITATIONAL FORCE AND POTENTIAL MODELS

We now list a number of models for the effective 2D planetary force or potential that we explore in this work.

First, the explicit form (18) of the initial density distribution in our disc allows us to compute a form of 2D acceleration \mathbf{a} under the assumption that ρ evolves away from ρ_0 only a little. The disc is acted on by the combined stellar and planetary gravitational potential, $\Phi = \Phi_\star + \Phi_p$, where $\Phi_\star = GM_\star/(R^2 + z^2)^{1/2}$, and

$$\Phi_p = \frac{GM_p}{(s^2 + z^2)^{1/2}}, \quad (20)$$

with s being the the polar distance between a point at (R, ϕ) and the planet at (R_p, ϕ_p) ,

$$s \equiv \sqrt{R^2 + R_p^2 - 2RR_p \cos(\phi - \phi_p)}. \quad (21)$$

We can now compute \mathbf{a} by vertically averaging the planetary²

² Formally, we should also vertically average the gravitational force due to the star. However, the effects of this averaging are only important within a few scale heights of the gravitational mass. We do not go this close to the star, and thus it is appropriate to approximate the stellar potential as Keplerian, depending only on R .

potential (20) over the density distribution (18). From the definition (14), the gravitational acceleration due to the planet is

$$\begin{aligned} \mathbf{a}_B \cdot \hat{R} &\equiv -\frac{1}{\Sigma} \int \rho \frac{\partial \Phi}{\partial R} dz \\ &= \frac{GM_p}{\sqrt{2\pi}H} \int \exp\left(\frac{-z^2}{2H^2}\right) \frac{R - R_p \cos(\phi - \phi_p)}{(s^2 + z^2)^{3/2}} dz \\ &= \frac{GM_p}{\sqrt{2\pi}H} \frac{R - R_p \cos(\phi - \phi_p)}{2H^2} e^y [K_0(y) - K_1(y)], \end{aligned} \quad (22)$$

$$\begin{aligned} \mathbf{a}_B \cdot \hat{\phi} &\equiv -\frac{1}{R\Sigma} \int \rho \frac{\partial \Phi}{\partial \phi} dz \\ &= \frac{GM_p}{R\sqrt{2\pi}H} \int \exp\left(\frac{-z^2}{2H^2}\right) \frac{RR_p \sin(\phi - \phi_p)}{(s^2 + z^2)^{3/2}} dz \\ &= \frac{GM_p}{\sqrt{2\pi}H} \frac{R_p \sin(\phi - \phi_p)}{2H^2} e^y [K_0(y) - K_1(y)], \end{aligned} \quad (23)$$

where $y \equiv s^2/4H^2$, and K_0 and K_1 are the zeroth and first order modified Bessel functions of the second kind. This force is equivalent to that derived by Müller et al. (2012, see their equations 17 and 20), and we will refer to it as the ‘Bessel-type force’ throughout the text.

In Appendix A, we obtain a slightly different from of the gravitational acceleration \mathbf{a} , which follows from an alternative derivation of the 2D fluid equations, based on linear mode decomposition. To disambiguate between these two prescriptions for \mathbf{a} , we refer to the force derived from linear mode decomposition by the symbol $\mathbf{a}_{B,\text{lin}}$.

4.1 Gravitational potentials in 2D discs

The 2D gravitational force prescriptions derived above are non-conservative, i.e. cannot be described as the gradient of a potential, except in the case of a constant scale height, see equation (17). However, it may be preferable to retain the conservative nature of gravity in 2D analysis (in Section 6, we will show that using the non-conservative force prescriptions leads to unexpected qualitative differences with the 3D case). In this section, we describe four different smoothed gravitational potentials that we later explore in our 2D simulations.

The first alternative potential we consider is that of Brown & Ogilvie (2024),

$$\Phi_{B,H_p} \equiv -\frac{GM_p}{H_p} \frac{e^{y_p}}{\sqrt{2\pi}} K_0(y_p), \quad (24)$$

where $y_p = s^2/(4H_p^2)$, $H_p = c_s(R_p)/\Omega_K(R_p)$. This version was derived in the shearing sheet approximation, and its use of H_p thus completely ignores the dependence of scale height H on R . If $H(R)$ were indeed constant and equal to H_p , then the acceleration due to this potential would be given by \mathbf{a}_B , see equations (22), (23).

Our second alternative potential is

$$\Phi_B \equiv -\frac{GM_p}{H} \frac{e^y}{\sqrt{2\pi}} K_0(y), \quad (25)$$

where $y = s^2/(4H^2)$, as in Equation (23). This form is the same as in Equation (24) except we now use the scale height as a function of R rather than using a fixed value of H_p . This potential can be derived either by dropping higher-order coupling terms in the linear mode analysis (Appendix A), or by simple, though not necessarily analytically supported, extension to the Brown & Ogilvie (2024) form.

In addition, we consider two traditional forms of the smoothed

potential. We use the second order smoothed potential as in Equation (1), and the fourth order smoothed potential (Dong et al. 2011a)

$$\Phi_4 \equiv -GM_p \frac{s^2 + 3r_s^2/2}{(s^2 + r_s^2)^{3/2}}. \quad (26)$$

Both forms rely on a choice of the smoothing length, r_s , which we parametrize as $r_s = bH_p$. The behaviour of these potentials, along with a Keplerian potential, is illustrated in Figure 1.

5 NUMERICAL METHODS

We perform a suite of 2D and 3D inviscid non-linear hydrodynamic simulations using ATHENA++ (Stone et al. 2020). ATHENA++ solves the hydrodynamic equations

$$\frac{\partial \rho}{\partial t} + \nabla \cdot (\rho \mathbf{v}) = 0, \text{ and} \quad (27)$$

$$\frac{\partial(\rho \mathbf{v})}{\partial t} + \nabla \cdot (\rho \mathbf{v} \otimes \mathbf{v} + P \mathbf{I}) = -\rho \nabla \Phi_\star + \rho \mathbf{g}, \quad (28)$$

in conservative form using a Godunov scheme, where P is the pressure, ρ the density, and \mathbf{v} is the velocity vector. Φ_\star is the gravitational potential of the central star. The body forces \mathbf{g} are calculated using either the gradient of a planetary potential $\mathbf{g} = -\rho \nabla \Phi_p$ or one of the acceleration prescriptions, \mathbf{a}_B and $\mathbf{a}_{B,\text{lin}}$, as described in Section 3.

We simulate a disc with aspect ratio $H_p/R_p = 0.05$ at the planetary location and planetary mass $M_p = 0.25M_{\text{th}}$, where $M_{\text{th}} = (H_p/R_p)^3 M_\star$ is the thermal mass. The planetary mass is in the weakly non-linear regime where the theory of Goodman & Rafikov (2001) and Rafikov (2002a) for the shocking of the planetary wake applies, however the mass is too large for linear Type I torque estimates to be valid (Masset et al. 2006). In line with previous papers, we choose not to include the indirect potential of the planet in our simulation³.

Our simulations span a large grid of temperature and surface density slopes. For surface density slopes $p \in \{0, 1.5\}$ we test temperature slopes $q \in \{0, 0.5, 1.0, 1.5, 2\}$ and for $p \in \{0.5, 1, 2\}$ we run only globally isothermal, $q = 0$, simulations. The globally isothermal simulations were computed using ATHENA++’s isothermal equation of state. Locally isothermal simulations were computed with the adiabatic equation of state with $\gamma = 1.0001$ and infinitely fast cooling to the background state⁴.

We cover the full 2π in azimuth and use a fiducial resolution of $N_\phi = 3600$ (approximately 28 cells per scale height at R_p) in both 2D and 3D runs. In Appendix B, we test the numerical convergence of our simulation with respect to grid spacing. We find that while the one-sided Lindblad torque is converged at this resolution, gap spacing was not. Nevertheless, as this resolution is already finer than many other papers in the literature, and as this paper is mostly concerned with the relationship between 2D and 3D simulations, this is a fine enough resolution as long as it is the same in both 2D and 3D simulations.

To avoid spurious shocks we ramp up the planetary mass sinusoidally over 10 orbits (equivalent to the ramping used in Cimerman & Rafikov 2021). We performed temporal convergence tests for a small number of our 2D simulations, and found that both torque and angular momentum deposition were converged at 10 orbits. In

³ Recently, Crida et al. (2025) showed that the indirect potential of the planet only weakly affects Type I migration rates.

⁴ Miranda & Rafikov (2019b) showed that there was a significant dynamical difference between using infinitely fast cooling and using only $\gamma \rightarrow 1$ to represent local isothermality.

3D, one-sided torques and horseshoe widths were converged at 10 orbits. The migration torque was not completely converged at this point, and it has been shown that multiple viscous timescales are required to reach convergence (D’Angelo & Lubow 2010). Therefore, we consider convergence within 5% across a few orbits to be acceptable (when we tested a viscous simulation we found that there was much better temporal convergence in the migration torque at this point, see Appendix B for further detail). With the exception of some unexpected structures within the horseshoe region (see Section 6.1.1), the deposition torque density $\partial F_{\text{dep}}/\partial R$ (see Section 5.3.2) was converged within 2.5 per cent compared to its maximum value by 10 orbits. At this time the maximum deviation in surface density due to gap opening was 0.3 per cent from the background, as such there are no concerns about instabilities such as the RWI setting in.

5.1 3D Simulations

Our 3D simulations used spherical co-ordinates, where $\{r, \phi, \theta\}$ are the radial, azimuthal and co-latitude co-ordinates respectively. Our logarithmically spaced radial grid spans from $0.4R_p$ to $2R_p$, and has damping zones for $R < 0.45$ and $R > 1.8$. The damping zones damp density and velocity to their initial conditions over a timescale of $0.25/\Omega_K$. In co-latitude the grid covered $\pi/2 - 3h_p$ to $\pi/2$, with the planet located at $\theta = \pi/2$ with reflecting boundary conditions. Our fiducial resolution is $N_r \times N_\phi \times N_\theta = 900 \times 3600 \times 156$.

We tested our simulations to ensure that covering a wider region in co-latitude, either by increasing the width above the midplane of this region or by covering both the upper and lower halves of the grid, did not significantly change our results.

Even though we do not have to physically smooth the planetary potential in 3D we still have to smooth it for practical numerical reasons. To do so we used the Φ_2 potential with a smoothing length of $b = 0.1$. This choice of smoothing length has been shown to have only sub-percent effects on the horseshoe width and torques (Masset & Benítez-Llambay 2016).

5.2 2D Simulations

In 2D, our logarithmically spaced radial grid spans $0.2R_p$ to $4R_p$ with damping zones for $R < 0.28R_p$ and $R > 3.4R_p$, arranged analogous to 3D. The grid is uniformly spaced in ϕ across 2π with periodic boundary conditions. Our fiducial resolution is $N_r \times N_\phi = 1800 \times 3600$.

We ran simulations with all of the 2D potentials and gravitational accelerations that were discussed in Section 3, i.e. \mathbf{a}_B , $\mathbf{a}_{B,\text{lin}}$, Φ_B , Φ_{B,H_p} , Φ_2 , & Φ_4 . We implemented the Bessel-type acceleration using Bessel function representation from the CEPHES Math Library (Moshier 1989). For Φ_2 , we tested smoothing lengths $b \in \{0.4, 0.6, 0.7, 0.9\}$. For Φ_4 , we tested smoothing lengths $b \in \{0.7, 1.1, 1.4\}$, but only performed globally isothermal simulations. A small number of additional tests were run with a wider range of smoothing lengths, however we do not include those in the discussion of this paper.

5.3 2D-3D comparison metrics

Similarity between the 2D and 3D results can be judged based on a number of criteria. In this work we consider several comparison metrics, which can be loosely grouped into two types based on their physical nature.

The first kind of metrics are based on the angular momentum exchange in the course of planet-disc interaction, and involves different types of torques. In locally isothermal discs, two types of torques are excited by planet-disc interactions. One are the Lindblad torques which excite density waves (a process characterized by the *excitation* torque density, see equations (30) and (31)) that subsequently travel radially away from the planet (Goldreich & Tremaine 1979). These density waves carry angular momentum which they deposit into the disc when they dissipate (a process characterized by the *deposition* torque density, see equation (33)). In a globally isothermal or adiabatic disc, this occurs due to shock formation (Goodman & Rafikov 2001; Rafikov 2002a), but in non-isothermal discs, dissipation can be caused by radiation or cooling (Miranda & Rafikov 2020; Ziampras et al. 2023). (In *locally* isothermal discs changes in background temperature can also lead to some angular momentum dissipation (Miranda & Rafikov 2019b), however, for the cases considered in this paper this type of dissipation is unimportant.)

Angular momentum exchange is also mediated by the co-rotation or horseshoe torque, which is limited in effect to a narrow region co-orbital with the planet. This torque is proportional to the local vortensity gradient, however in inviscid discs horseshoe motion quickly leads to an averaging of vortensity across this region (Balmforth & Korycansky 2001) saturating the torque (Ward 1991; Masset 2002; Masset et al. 2006; Masset & Benítez-Llambay 2016). In non-isothermal discs, other torques can be excited, including buoyancy torques (Zhu et al. 2012; McNally et al. 2020; Ziampras et al. 2024b), thermal torques due to planetary luminosity (Benítez-Llambay et al. 2015) and radiative cooling within the horseshoe region (Lega et al. 2014; Ziampras et al. 2024a).

The second type of metrics that we use are based on the structures that form in the disc as a result of planet-driven density wave dissipation. The dissipation of the wave angular momentum into the disc causes disc to evolve and gaps to form (e.g. Rafikov 2002b; Kanagawa et al. 2015; Cordwell & Rafikov 2024, hereafter CR24). The detailed shapes of the gaps can also be compared between the 2D and 3D simulations, providing us with another kind of metric.

The metrics we use have different dimensionality. We use 2D and radial 1D metrics in order to understand some qualitative differences, and we also use integrated single value (summary) metrics to numerically quantify the performance of different acceleration/potential prescriptions. These summary values are also used to calculate optimal smoothing lengths for Φ_2 and Φ_4 .

5.3.1 2D Metrics

We use two 2D metrics to understand the qualitative behaviour of the simulations. First, we use Σ/Σ_0 , the normalised surface density, and secondly we look at vortensity, ζ . In 2D simulations this is defined as $\zeta = \nabla \times \mathbf{u}/\Sigma$, and for 3D simulations we use the Masset & Benítez-Llambay (2016) definition,

$$\zeta_{3D} = \left[\int_{-\infty}^{\infty} \left(\frac{\rho}{(\nabla \times \mathbf{v})_z} \right) dz \right]^{-1}. \quad (29)$$

5.3.2 Radial Metrics

We use azimuthally-integrated 1D radial metrics to directly compare between 2D and 3D simulations:

- Firstly, we consider the excitation torque density, i.e. the amount of torque excited gravitationally by the planet per unit radius. In 2D

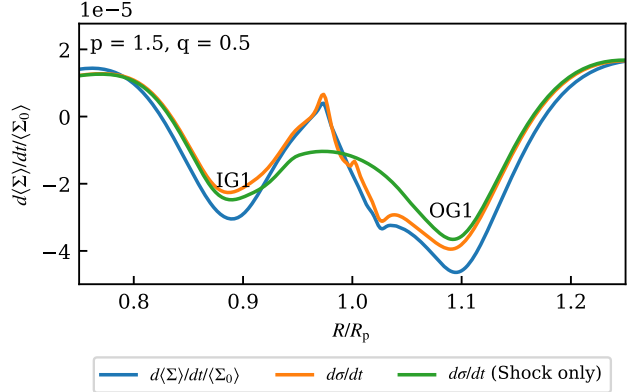


Figure 2. 1D profile of the surface density evolution measured from a 3D simulation, $\langle \Sigma_0 \rangle^{-1} d\langle \Sigma \rangle / dt$, compared to the expected Σ evolution, $d\sigma / dt$, using the theory of CR24, with F_{dep} measured from the simulation. This run used power law indices of Σ and T of $p = 1.5$ and $q = 0.5$. We also show the evolution expected if we set F_{dep} to zero within one scale height of the plane, $d\sigma / dt$ (shock only), which describes the evolution caused by the shocking of the planetary wake only (i.e. with co-rotation effects removed). The labels IG1 and OG1 refer to the locations of the inner and outer gaps closest to the planet, and are used to determine gap spacing. Despite some quantitative differences in gap depth between the measured and theoretical Σ evolution, the theory of CR24 is clearly applicable to the 3D case.

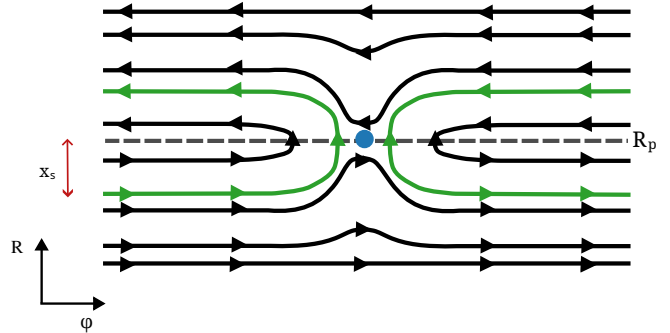


Figure 3. A sketch of fluid streamlines within the frame co-rotating with the planet. Close to the radial location of the planet the gas will undergo horseshoe turns on closed loops. The width of this region is key in determining the magnitude of the co-orbital torque (e.g. Brown & Ogilvie 2024). The horseshoe width, x_s , is the radial distance between R_p and the most radially distant streamline that undergoes a horseshoe turn (shown in green).

disks this is defined as

$$\frac{\partial T}{\partial R} \equiv -R \oint \Sigma(R, \phi) \frac{\partial \Phi_p}{\partial \phi} d\phi, \quad (30)$$

and in 3D the equivalent definition is

$$\frac{\partial T}{\partial R} \equiv -R \oint \int_{-\infty}^{\infty} \rho \frac{\partial \Phi}{\partial \phi} dz d\phi. \quad (31)$$

For 3D discs, we also define the ‘2D Mode’ of the torque as

$$\frac{\partial T}{\partial R} \Big|_{2D} \equiv -R \oint \left(\int_{-\infty}^{\infty} \rho dz \right) \frac{\partial \Phi_B}{\partial \phi} d\phi. \quad (32)$$

This is derived from the lowest order mode of the vertical mode analysis in Appendix A. Equation (32) therefore represents the amount

of torque that would be excited if the vertical structure of the disc remained as in Equation (18).

- Secondly, we consider the angular momentum deposition function,

$$\frac{dF_{\text{dep}}}{dR} = \frac{\partial T}{\partial R} - \frac{\partial F_{\text{wave}}}{\partial R}, \quad (33)$$

where F_{wave} is the amount of angular momentum carried in the planet-driven density wave. For 2D discs,

$$F_{\text{wave}} \equiv \oint \Sigma u_R \delta u_\phi d\phi, \quad (34)$$

where $\delta u_\phi \equiv u_\phi - (\oint \Sigma d\phi)^{-1} \oint \Sigma u_\phi d\phi$ as per CR24. In 3D discs,

$$F_{\text{wave}} \equiv R^2 \oint \int_{-\infty}^{\infty} \rho v_R \delta v_\phi dz d\phi, \quad (35)$$

where $\delta v_\phi \equiv v_\phi - (\oint \int_{-\infty}^{\infty} \rho dz d\phi)^{-1} \oint \int_{-\infty}^{\infty} \rho v_\phi dz d\phi$. A derivation for this metric in 3D discs is included in Appendix C.

- Thirdly, we consider the azimuthally averaged surface density evolution,

$$\frac{d\langle \Sigma \rangle}{dt} \frac{1}{\langle \Sigma_0 \rangle} = \frac{\langle \Sigma(t = 11P_p) \rangle - \langle \Sigma(t = 10P_p) \rangle}{\langle \Sigma_0 \rangle}, \quad (36)$$

where $\langle \dots \rangle$ represents azimuthal averaging. In the initial stages of gap-opening surface density evolution is linear in time (CR24), and as such the period separated difference is representative of the instantaneous derivative on the LHS of this equation.

- Lastly, we calculate the expected surface density evolution if the co-rotation torque were saturated. The co-rotation torque saturates over the course of a few libration timescales, and as such it will not impact long term gap growth. For the planetary mass and thermodynamic equation of state used in this paper, the excited planetary wakes do not dissipate their angular momentum until they are over a scale height away from the location of the planet (Goodman & Rafikov 2001). As such, any angular momentum deposition within a scale height of the planet will be caused by the co-rotation torques⁵.

CR24 derived a procedure to calculate gap evolution expected for a given function $\partial F_{\text{dep}}/\partial R$. Therefore, we can remove the angular momentum deposition in the co-orbital region from a measured $\partial F_{\text{dep}}/\partial R$ and use this new, ‘shock-only’, angular momentum deposition function to generate a ‘shock-only’ gap evolution profile, $d\sigma/dt$ (shock only). We do this by setting $\partial F_{\text{dep}}/\partial R$ to zero within one scale height from R_p and then passing it through the machinery of CR24.

CR24 developed their framework for 2D discs, and only tested their theory using semi-analytic formulae for angular momentum deposition obtained in Cimerman & Rafikov (2023). To ensure that their machinery can be applied to 3D, we re-derive the 1D equations of angular momentum transport in 3D discs in Appendix C. We also performed tests of their method using $\partial F_{\text{dep}}/\partial R$ as measured from simulations, we show this Figure 2. This figure also displays the difference between $d\sigma/dt$ (shock only) and $\langle \Sigma_0 \rangle^{-1} d\langle \Sigma \rangle/dt$.

These 1D measures are all known to be approximately constant in time for the early stages of gap opening in 2D simulations (Cordwell & Rafikov 2024; Cimerman & Rafikov 2021), and we tested that this temporal invariance was still true in 3D simulations.

⁵ This is a slight oversimplification. In locally isothermal discs, F_{wave}/c_s^2 , rather than F_{wave} as in globally isothermal or adiabatic discs, is conserved (Miranda & Rafikov 2019a). However, as we are only considering a small area of the disc, where c_s^2 does not change significantly, conservation of F_{wave} in the co-orbital region is a valid assumption.

5.3.3 Summary Metrics

Our final set of metrics are individual numbers which we use to summarize and quantify our results. The first two summary metrics are derived from the excited torque, the third relates to $d\sigma/dt$ (shock only) as defined above, and the last relates to the velocity structure in the co-rotation region.

- Our first summary metric is the total excited (migration) torque,

$$T/T_0 = \int_0^\infty (\partial T/\partial R) dR, \quad (37)$$

where $\partial T/\partial R$ is defined in Equation (30) or Equation (31) for 2D or 3D discs respectively. The normalization value,

$$T_0 = \left(\frac{M_p}{M_\star} \right)^2 h_p^{-2} \Sigma_p R_p^4 \Omega_p^2, \quad (38)$$

is the expected scaling from linear theory (Goldreich & Tremaine 1980). A positive value of T represents a torque that causes inward migration of the planet. For our 3D simulations we will sometimes also show the equivalent as calculated from the 2D mode, where $T_{2D} \equiv \int_0^\infty (\partial T/\partial R)|_{2D} dR$.

- The second summary metric is the one-sided Lindblad torque,

$$T_{\text{OSL}}/F_{\text{J},0} = \frac{1}{2} \left(\left| \int_0^{R_p} (\partial T/\partial R) dR \right| + \left| \int_{R_p}^\infty (\partial T/\partial R) dR \right| \right), \quad (39)$$

where the normalization term is

$$F_{\text{J},0} = \left(\frac{M_p}{M_\star} \right)^2 h_p^{-3} \Sigma_p R_p^4 \Omega_p^2. \quad (40)$$

This is the classic scaling of the one-sided planet-driven Lindblad torque from Goldreich & Tremaine (1980). In 3D, we also define $T_{\text{OSL}}|_{2D}$ analogously to T_{2D} . T_{OSL} describes the overall magnitude of the interaction and determines gap depths at viscous steady state (Kanagawa et al. 2015).

- The third summary metric is initial gap spacing. In inviscid discs planet-opened gaps initially have a double minima structure, one on each side of the planet. The spacing between these gaps, and more specifically the dust gaps they cause, is expected to be a good probe of a planetary mass from observations (Dong et al. 2015). For this metric we adopt

$$\frac{R_{\text{OG1}} - R_{\text{IG1}}}{R_p}, \quad (41)$$

where R_{OG1} is the closest local minima to the planet in σ for $R > R_p$, and R_{IG1} is the equivalent for $R < R_p$. We show an example of gap structures, with these locations labeled, in Figure 2. As gap opening is a secular long term effect, the short term saturated horseshoe torque will not strongly affect the overall gap structure. Therefore we calculate gap spacing from $d\sigma/dt$ (shock only) so that it represents only Lindblad wake driven evolution.

- Lastly, we consider the horseshoe half-width, x_s (e.g. Masset & Benítez-Llambay 2016). In the frame co-rotating with the planet there exist a class of streamlines near R_p that, instead of passing the location of the planet azimuthally, perform a horseshoe turn and reverse their azimuthal velocity. We show a schematic of these streamlines in Figure 3. The horseshoe half-width is the radial distance between R_p and the furthest streamline that undergoes one of these horseshoe turns. We calculate this by evaluating streamlines from (vertically averaged) velocities calculated using SciPy’s solve_ivp function.

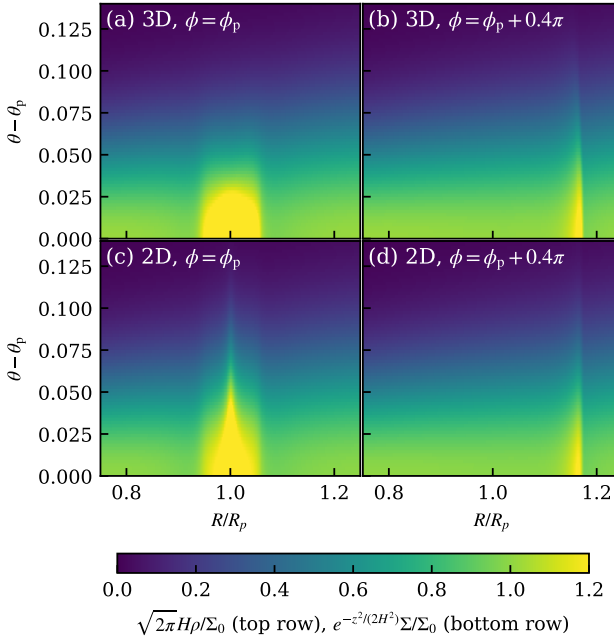


Figure 4. Vertical density slices from a $p = 1.5$ and $q = 0$ 3D simulation along lines of constant azimuth. Panels (a) & (b) show the full 3D structure, which is compared with the density structure derived from an equivalent 2D model in panels (c) & (d). The structure derived from 2D model is calculated as the surface density of the 3D model multiplied by $e^{-z^2/2H^2}$, i.e. the initial hydrostatic vertical density (18). In (a) and (c), where hydrostatic envelope around the planet is shown, it is clear that the 2D model misrepresents the planetary atmosphere. In (b) and (d), we compare the structure of the planet induced wake at a distance away from the planet. In the full 3D case, the wave curves slightly backwards towards the planet at higher altitudes whereas in the quasi-2D case the wake is required to be vertically straight.

5.4 Analysis software pipeline

In order to calculate all of the above described metrics, we developed an interoperable analysis software pipeline that works for 2D and 3D simulations. So far, this has been tested on both ATHENA++ and PLUTO simulations. The package is easily extendable to include output from other simulation codes, such as FARGO3D, as well as the inclusion of other physics (e.g. moving or eccentric planets). To allow other researchers to easily use the same metrics we have made this package available on GitHub, https://github.com/cordwella/disc_planet_analysis, under the MIT Open Source License.

6 RESULTS

This section, which describes our simulation results, is organised as follows. First, we describe the qualitative features of 3D simulations and show how these differ from what is represented by either the vertical average of that 3D simulation or a ‘literature standard’ 2D simulation that uses the second order potential Φ_2 , $b = 0.7$. Second, we show results from 2D simulations using the new physically motivated 2D gravitational acceleration prescriptions from Section 2, and compare these to 3D simulations. Lastly, we show results from 2D simulations using existing smoothed potentials, Φ_2 and Φ_4 , and use these to calculate optimal smoothing lengths for different physical features. We show results measured at 10 planetary orbits from the

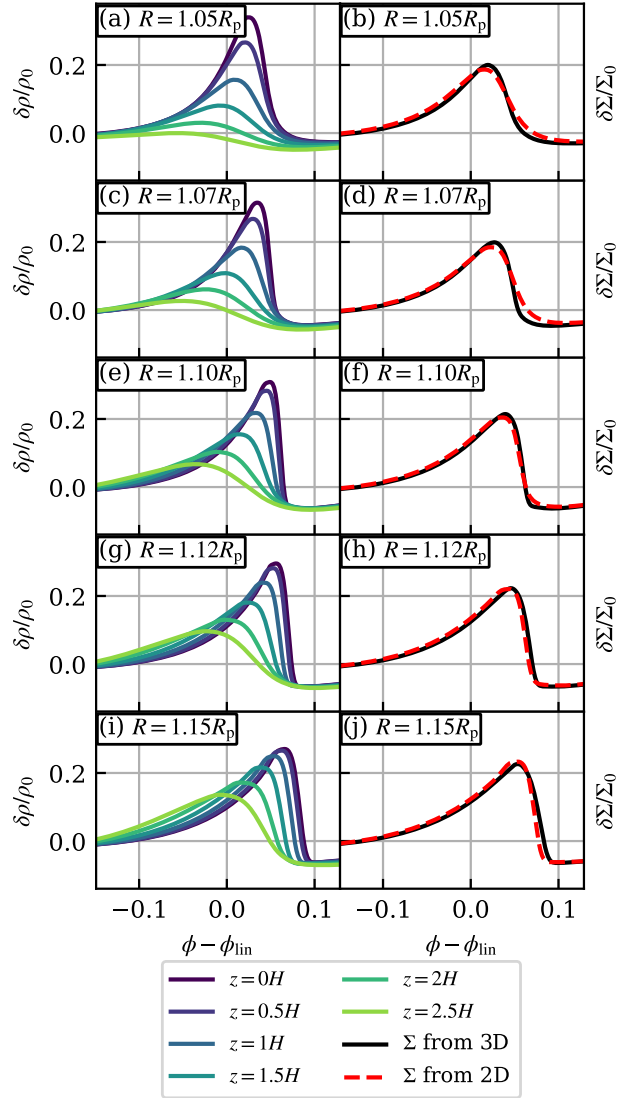


Figure 5. Left: Planet induced wake structure as a function of altitude above the midplane in the outer disc as measured from a 3D simulation ($p = 1.5, q = 0$). Right: Wake structure in surface density for the same 3D simulation compared to that from a 2D simulation using the potential $\Phi_2, b = 0.7$. The 3D wake structure is dependent on altitude, and shocks, identified visually as when the gradient of $\delta\rho/\rho_0$ reaches its maximum, form at the midplane radially sooner (e) than at higher altitudes. The exact formation of the shock is not captured by the surface density evolution, and the literature standard 2D simulation shows slightly different shock formation and structure compared to the 3D case.

start of the simulation. In Appendix B, we check that this time is sufficient for temporal convergence.

6.1 The 3D nature of planet–disc interactions

To situate ourselves in the problem, we first examine the key features of the 3D planet–disc interaction that are or are not reproduced by a 2D calculation..

In Figure 4, we show azimuthal slices of the density distribution from a 3D simulation (top row) and compare this to the ‘recon-

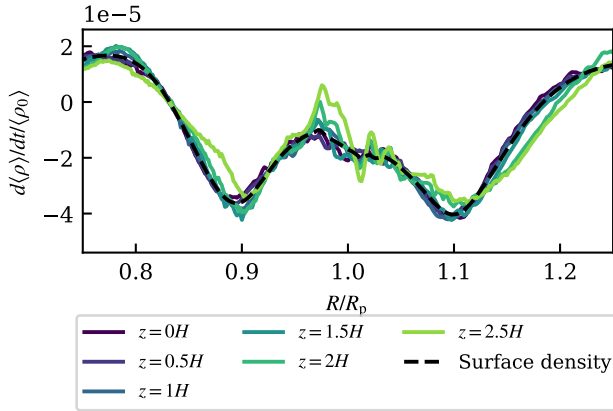


Figure 6. Time derivative of density from our fiducial 3D simulation as a function of altitude above the midplane (solid lines) compared to the time derivative of surface density (dashed line). Within a scale height of the midplane, density evolution is very similar to surface density evolution however at higher altitudes gap formation in the outer disc happens further away from the planet.

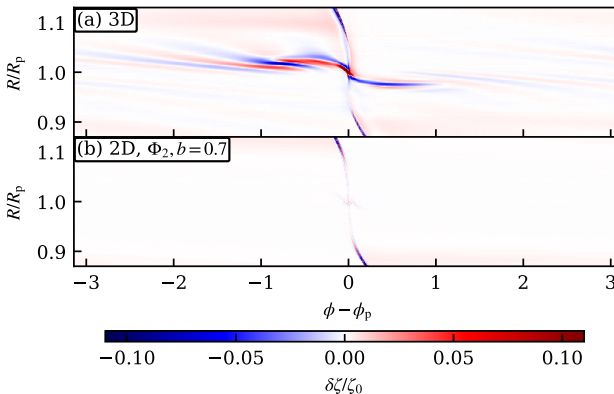


Figure 7. Map of vortensity ζ_{3D} defined by equation (29) based on our fiducial 3D simulation (a) compared with the vortensity map from an equivalent 2D simulation (b). In 2D, vortensity ζ is constant within the horseshoe region. However in the 3D simulation, stripes of vortensity are generated in the horseshoe region near to the planet.

structed’ density structure (bottom row) that would be implied by a 2D calculation if one were to make an assumption of a vertical hydrostatic equilibrium. In practice, this means that one assumes $\rho(z) = \rho_0(z)$ given by the equation (18) with Σ_0 equal to the local Σ from a 2D run. Such 3D density ‘reconstruction’ from 2D data has been attempted in the past (e.g. Zhu et al. 2015; Dong et al. 2017).

Two differences between the true and reconstructed ρ should be emphasized. First, the reconstructed model is unable to account for the near-spherical planetary atmosphere that forms in 3D, see panels (a) and (c). Second, the form of the density wave in panel (b) curves towards the planet as altitude increases (see also Figure 5) — obviously this is not reproduced in 2D (panel (d)), and therefore causes the 2D equivalent to form a less distinct shock edge.

In Figure 5 we investigate the structure of the planet-driven density wake in more detail. In the 3D case, the relative amplitude of the density perturbation $\delta\rho/\rho_0(z)$ strongly decays with the height z above

the midplane, at all R . This is caused by weakening of the planetary potential, to which the wake couples at excitation, with z . As the distance from the planet increases, the wake steepens due to nonlinear effects at all heights, but much faster closer to the midplane. As a result, when the wave eventually shocks⁶, this happens first near the midplane, where the wave is more nonlinear. The wake eventually shocks at all measured altitudes, however the distance away from the planet at which the shock occurs increases with altitude.

In the right column we show how the wake shows up in Σ and compare it to a 2D simulation. Despite the wake from both types of simulations being similar in magnitude one scale height away from the planet (Figure 5 (b)), in the 3D simulation the wake shocks earlier, (Figure 5 (d)), than in the 2D simulation (Figure 5 (h)).

To ensure that 3D gap evolution occurs similarly to 2D gap formation, we illustrate density evolution, expressed as a time derivative of $\rho(z)$, as a function of altitude z in Figure 6. We find mostly very similar evolution at different altitudes, although the outer gap forms further away from the planet at higher altitudes. This difference is likely due to shock formation occurring at further distances from the planet at higher altitudes, as shown in Figure 5, and therefore angular momentum deposition occurring further away from the planet. There are also unexpected features, more present at higher altitudes, which we believe to be caused by 3D motion, and in particular what we will call ‘horseshoe vortensity striping’, discussed next.

6.1.1 Horseshoe vortensity striping

In Figure 7, we show a maps of vortensities ζ and ζ_{3D} (defined by equation (29)) from a pair of 2D and 3D simulations. Both simulations have an initially flat vortensity ($p = 1.5$) and temperature profile. In 2D the bulk vortensity only evolves after the planetary wake has shocked (i.e. $R < 0.9R_p$), as expected from previous work (e.g. Li et al. 2005; Dong et al. 2011b; Cimerman & Rafikov 2021). However in 3D, large scale stripes of 3D vortensity ζ_{3D} form in the horseshoe region, see panel (a). We verified that we see such stripes also in the map of z -component of the conventional vortensity ζ_z at $z = 0$. These features are especially prominent in the region where fluid parcels exit their horseshoe turn close to the planet (in this simulation the horseshoe region ranges from $0.975R_p$ to $1.025R_p$). We allowed this simulation to run for longer and found that while the shape of the structure did not change in time, it grew in magnitude. In surface density, this feature can also be seen in non-axisymmetric stripes of material, but the magnitude of this effect is much smaller than that of shock driven gap opening.

Horseshoe vortensity striping has been previously observed by Masset & Benítez-Llambay (2016) and Chametla et al. (2025). They claimed that this feature is caused by horseshoe streamlines bending vertically down to the planet at closest approach. Vortensity is a conserved quantity in 2D, a property that would hold if planet–disc interactions remained fundamentally 2D in 3D simulations. Clearly this interaction is 3D enough for vortensity not to be conserved, which may have implications for features that have long been studied from the perspective of vortensity, such as the dynamical co-rotation torque (Masset & Papaloizou 2003).

⁶ In this paper we visually identify a shock location by when the gradient of $\delta\rho/\rho_0$ reaches its maximum and there is a clear ‘knee’ break between the front of the wake and the background disc. In a 2D isothermal disc it is possible to use the perturbed vortensity structure to identify the location that the shock forms (Cimerman & Rafikov 2021), however this is infeasible to use in 3D due to the formation of ‘horseshoe vortensity stripes’, see Section 6.1.1.

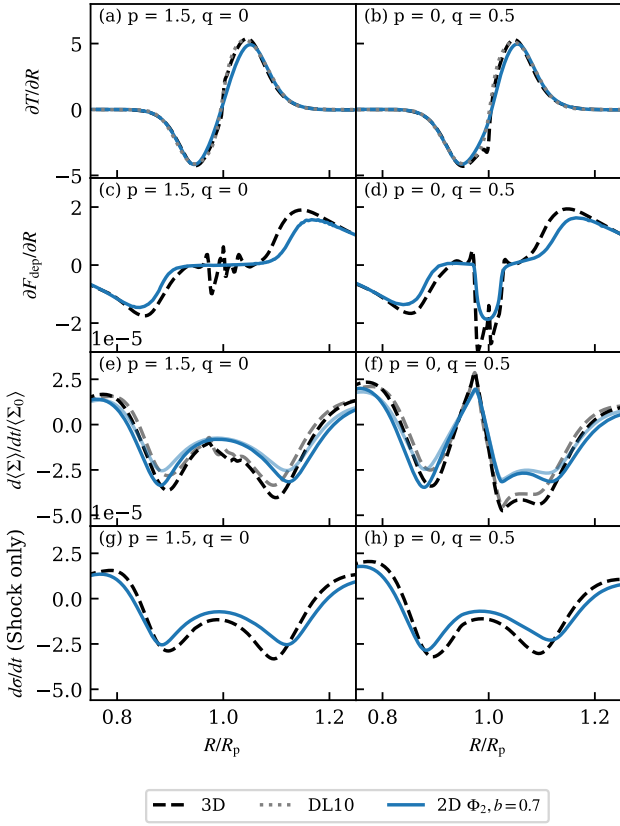


Figure 8. Radial metrics as measured from 3D (dashed lines) and 2D (solid lines) simulations. The 2D simulations use second order potential Φ_2 , $b = 0.7$. The simulations in the left-hand column have background surface density and temperature gradients of $p = 1.5$ and $q = 0$. Those in the right-hand column have $p = 0$ and $q = 0.5$. Each row shows a different radial metric as defined in Section 5.3.2. The first two rows show the torque excited by the planet and angular momentum deposition respectively (in units of $F_{J,0}$). The first row also shows the expected excitation profile from the viscous simulations of D'Angelo & Lubow (2010). The third row shows surface density evolution as measured from the simulation, and in matching lighter colours the expected evolution using the theory of CR24 with the measured F_{dep} from the row above. The final row shows the expected surface density evolution if $\partial F_{\text{dep}}/\partial R$ was zero within 1H of the planet. See Section 5.3.2 for further detail on the metrics and the text for further discussion.

As horseshoe vortensity striping has not yet been widely discussed, we also undertook a series of tests to ensure that it was not numerical in origin. The structure was unchanged by differences in planetary ramp up time, or the nature and position of vertical boundaries. Using a smaller planetary mass changes the number of stripes but does not stop the effect from occurring. Including a viscosity in the simulation (we tested $\nu = 2.5 \times 10^{-6}$), increasing the 3D smoothing length, or disconcertingly, increasing the local grid resolution, all caused the magnitude of this structure to decrease. This feature is clearly not numerical, although its convergence properties remain to be established.

6.2 Radial metrics in 3D discs

Having discussed some fundamentally 3D parts of the planet-disc interaction, we now shift our focus to considering the radial metrics as defined in Section 5.3.2. In Figure 8, we compare representative

3D simulations with 2D simulations that use the second order potential Φ_2 with $b = 0.7$. The expected difference between the two representative choices of background surface density and temperature profiles is whether or not the co-rotation torque should be active. Indeed, for the $p = 1.5, q = 0$ simulations the co-rotation torque is not active and angular momentum deposition peaks away from the planet, at $R \approx 0.85$ and $R \approx 1.1$ in Figure 8(c), as expected from weakly non-linear shocking (Goodman & Rafikov 2001; Rafikov 2002a; Cimerman & Rafikov 2021). Whereas in the $p = 0, q = 0.5$ simulations the co-rotation torque is active and unsaturated, leading to angular momentum deposition in the horseshoe region. However, once the effect of the co-rotation torque is removed as in panels (g), (h), the expected gap profiles are similar for both simulations regardless of their p and q .

When comparing 2D and 3D simulations, the only qualitative difference between is due to horseshoe vortensity striping, the effect of which is limited to near the co-rotation region. At the quantitative level, there are differences dependent on the choice of smoothed potential, which we will investigate in Sections 6.3 and 6.4. However the analysis of the fundamental 3D structure of the planet-generated wake and shock suggest that even 2D simulations that correctly reproduce the initial excited structure of a planetary wake are unable to quantitatively capture the correct shock evolution, and therefore angular momentum deposition profile. Generally this leads to angular momentum deposition closer to the planet than in the 2D case thus leading to slightly smaller spacings between gaps.

We also compare our torque excitation with the models of D'Angelo & Lubow (2010). In Figure 8(b), while our 3D $\partial T/\partial R$ and the reference model of D'Angelo & Lubow (2010) match well for the majority of the radial domain, our simulation shows an additional spike in excited torque for R just under R_p . On further investigation we saw this feature in the low viscosity simulations of D'Angelo & Lubow (2010) (Fig. 5), and given that this is a 3D-only feature we believe it may be related to the horseshoe vortensity striping as described above.

We also checked how much angular momentum flux was carried in 2D versus 3D wave structures, i.e. the wave as measured from the vertically averaged velocity and density structures compared to the total wave angular momentum flux. We found that the 2D wave carried around 90% of the total wave angular momentum flux (matching theoretical predictions from Takeuchi & Miyama 1998), but that this proportion was not radially constant. Angular momentum can be transferred between different vertical modes of the wave, and so the 2D wave cannot be treated as independent of higher order vertical modes, i.e. changes in vertical structure.

In Appendix D, we use our large grid of 3D simulations to show how all radial metrics are affected by changing the slope parameters p and q .

6.3 2D simulations with Bessel-type forces and potentials

We now consider how well 2D simulations, using physically motivated (Bessel-type) gravitational accelerations, compare with 3D simulation results. In Section 2, we described two physical forms of the 2D gravitational force due to a planet from the 3D Navier-Stokes equations, \mathbf{a}_B and $\mathbf{a}_{B,\text{lin}}$, and two gravitational potential functions inspired by those, Φ_B and Φ_{B,H_p} . Our naive computational implementation for the Bessel-type forces and potentials leads to around a 20 per cent computational overhead compared to the second order smoothed potential.

We display radial metrics for a selection of these simulations in Figure 9. Panels (a) and (b) show a good match between 2D and

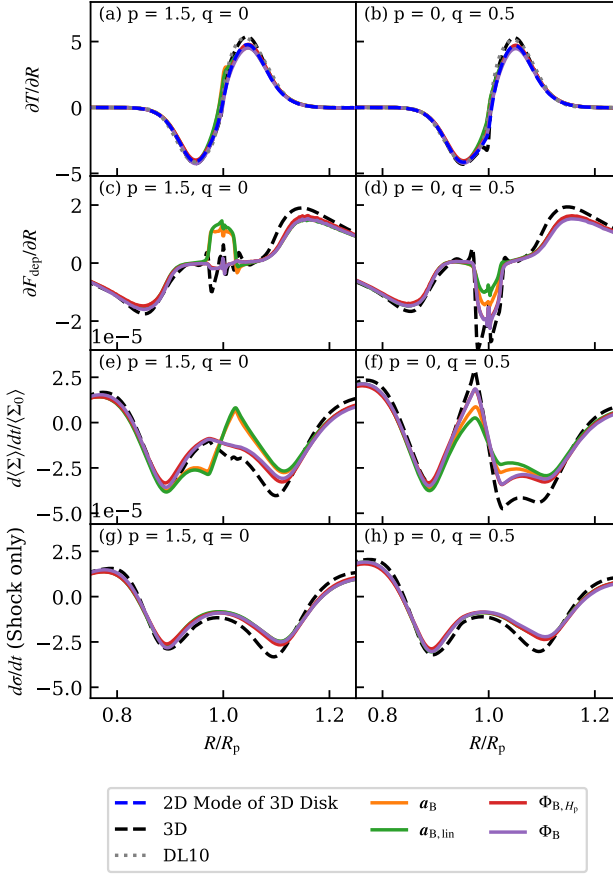


Figure 9. Same as Figure 8, except comparing the 3D results with 2D results using different Bessel-type forces (as defined in Section 2). In panels (a) and (b) we also include the 2D mode of the torque from the 3D simulations as defined in Equation (32). From top to bottom the rows represent excited torque, angular momentum deposition, measured surface density evolution, and expected surface density evolution in the absence of horseshoe effects.

Table 1. Comparison of key values from 2D simulations using the Bessel-type gravitational forces with 3D simulations. The values presented here have been averaged across simulations with different background gradients of p and q . The migration torque is omitted as it has a strong dependence on background gradients. Brackets indicate the torque from the 2D mode of the 3D simulation.

	$T_{\text{OSL}}/F_{\text{J},0}$ ($T_{\text{OSL}} _{2\text{D}}/F_{\text{J},0}$)	$(R_{\text{OG1}} - R_{\text{IG1}})/R_p$	x_s
3D	0.379 (0.345)	0.191	0.025
$\mathbf{a}_{\text{B,lin}}$	0.338	0.215	0.024
\mathbf{a}_{B}	0.338	0.215	0.024
Φ_{B}	0.339	0.215	0.024
Φ_{B,H_p}	0.341	0.215	0.024

3D simulations in the shape of $\partial T/\partial R$, although generally the 2D simulations have a lower peak torque excitation in the outer disk. When we consider the 2D mode of the 3D torque, $\partial T/\partial R|_{2\text{D}}$ given by equation (32), we find that these torque structures have an even better match. The small, but not inconsequential difference, is expected and represents the fact that gravitational acceleration and excited torque are affected by perturbations in the vertical structure of the disc, see Section 2. We should, therefore, not expect 2D simulations, which

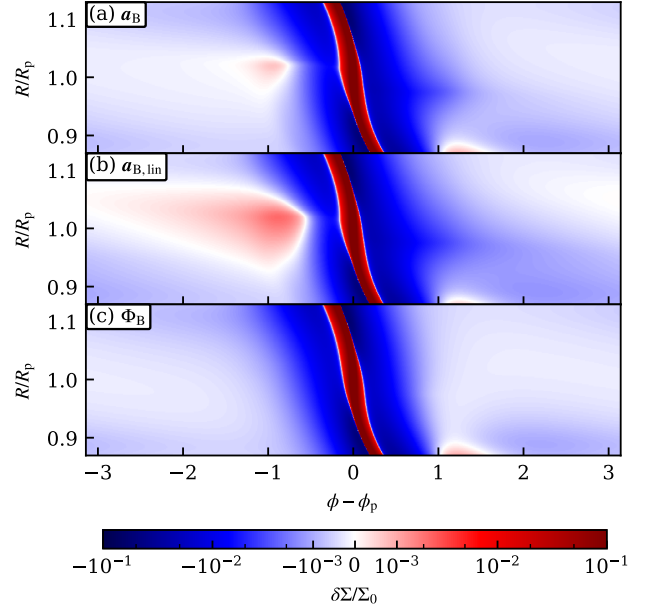


Figure 10. Maps of surface density in the co-orbital region around the planet for three different 2D simulations, with background gradients $p = 1.5, q = 0$, using gravitational force descriptions of \mathbf{a}_{B} , $\mathbf{a}_{\text{B,lin}}$ and Φ_{B} respectively. For this background state the co-rotation torque is expected to not be excited, and all of the evolution (once the density wakes are set up) should be driven by the shocks that occur outside this area. These discrepancies suggest that \mathbf{a}_{B} and $\mathbf{a}_{\text{B,lin}}$ are inappropriate choices for future 2D simulations, whereas Φ_{B} is a qualitatively appropriate choice.

assume no perturbation to the disc vertical structure, to be able to completely match torque values from 3D discs.

In angular momentum deposition, Figure 9 (c, d), simulations using \mathbf{a}_{B} and $\mathbf{a}_{\text{B,lin}}$ strongly deviate from behaviour expected in the co-rotation region from 3D runs. No 2D simulation is able to represent the effect of horseshoe vortensity striping, however using \mathbf{a}_{B} and $\mathbf{a}_{\text{B,lin}}$ results in yet additional density substructures in the co-orbital region, as we illustrate further in Figure 10. With the exception of the Lindblad wake centred at R_p , the surface density in the co-rotation region should be axisymmetric, but both \mathbf{a}_{B} and $\mathbf{a}_{\text{B,lin}}$ cause the formation of over and under-densities which seem to be centred around the location of the widest horseshoe turn. It is likely that these occur due to the non-conservative nature of the 2D forces used – in 3D these additional force components may be what leads to the horseshoe vortensity striping feature. We allowed some of these simulations to run for longer to ensure that this non-axisymmetric feature wasn't a transient effect. While the non-axisymmetric lobes are less visible in 2D plots at later times, the effect on angular momentum deposition and the azimuthally averaged surface density evolution was unchanged. Due to this effect, we conclude that neither \mathbf{a}_{B} nor $\mathbf{a}_{\text{B,lin}}$ should be used to represent planet–disc physics in a 2D simulation.

On the other hand, it is worth noting that when we re-calculate expected surface density evolution with the co-rotation effects removed, Figure 8(g, h), we see that the gap profiles are very similar for all Bessel-type accelerations and potentials.

2D simulations using Φ_{B} and Φ_{B,H_p} have, with the exception of missing the vortensity striping feature, good qualitative agreement with 3D simulations for all the metrics shown in Figure 9. Quantitatively, they miss some torque excitation, which must be associated

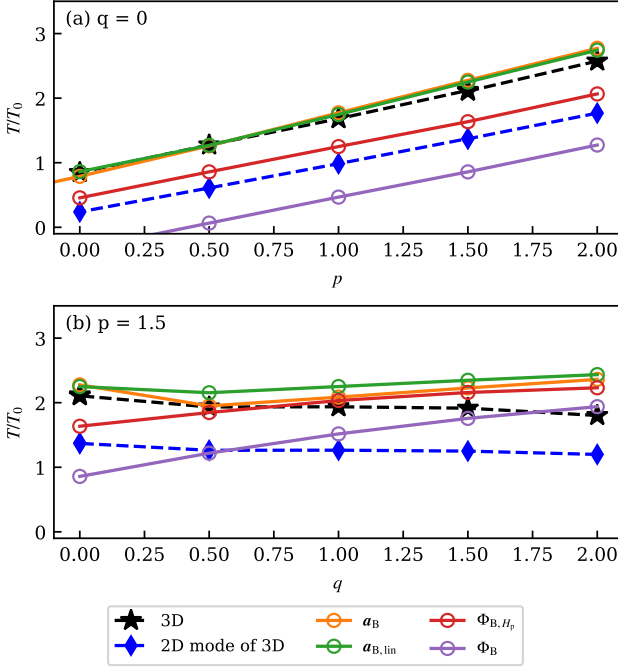


Figure 11. Total (migration) torque on the planet from 2D simulations using different Bessel-type forces (solid lines) compared to that from 3D simulations (dashed lines) as a function of surface density gradient p for a globally isothermal disc (a) and of temperature gradient q (b). The black dashed line and stars represent the 3D torque as measured directly from the simulation whereas the blue line and diamond represent the 2D mode of the torque (see Section 5.3.3 for a description). a_B is able to give the best 2D representation of the 3D migration torque, however, as shown in Figure 10, it is an inappropriate choice to match the qualitative features of surface density evolution.

with 3D vertical modes, and their predicted gap locations are slightly further away from the planet, but insomuch as possible for a 2D simulation, they represent the physics of the interaction well.

Out of our summary metrics we found that T_{OSL} , gap spacing, and horseshoe width, x_s , were mostly invariant under the choice of surface density and temperature slope, whereas – as expected from previous work and linear theory – the migration torque is strongly dependent on p and q . We show the average summary metrics in Table 1, with the exception of migration torque. All of our Bessel-type forces underestimate the one-sided Lindblad torque by around 10 per cent, although if we compare them instead to the 2D mode of the 3D torque they match within 3 per cent. Gap spacings from 2D simulations tend to be overestimated by around 8 per cent compared to 3D simulations, and 2D horseshoe widths are underestimated by 8 per cent.

In Figure 11, we compare migration torques between 3D and Bessel-type 2D simulations. a_B and $a_{B,\text{lin}}$ provide the best matches to the 3D migration torques, however these misrepresent much of the other physics of the interaction. Neither Φ_B nor Φ_{B,H_p} matched migration torque values well, although they were able to match the gradient of the torque with respect to p . None of these 2D prescriptions were able to match the gradient of the torque with respect to the background temperature slope q .

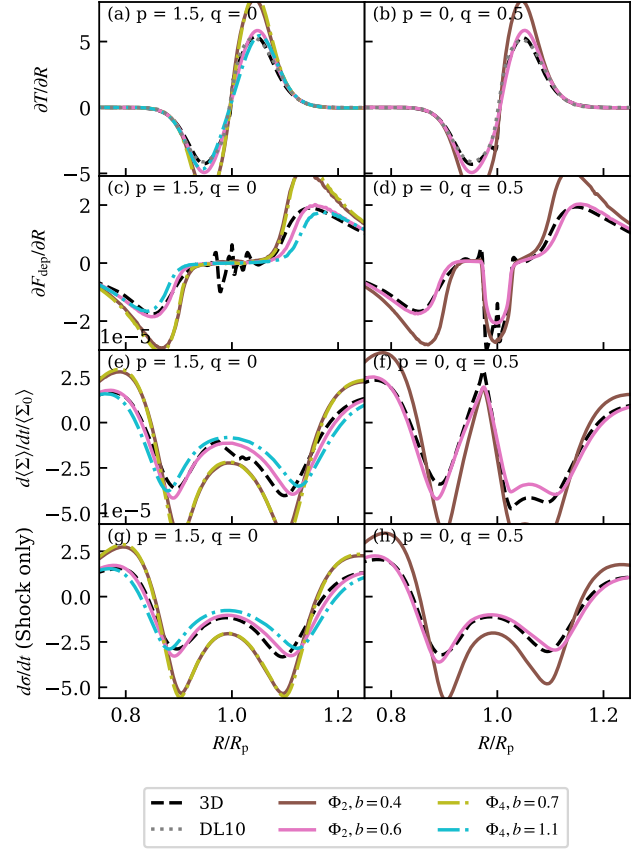


Figure 12. Same as Figure 8, except these now compare the same 3D results with 2D simulations using the second or fourth order smoothed potentials with different smoothing lengths. The fourth order potential was only used in globally isothermal simulations and as such is not included in the right column. As before, from top to bottom the rows represent excited torque, angular momentum deposition, measured surface density evolution, and expected surface density evolution in the absence of horseshoe effects.

Table 2. Optimal smoothing lengths, $b = r_s/H$, for traditional potentials in 2D simulations, calculated by comparison to the same metric in 3D simulations. No optimum b is provided for migration torque as the optimum is strongly dependent on the choice of background gradients.

T	T_{OSL}	$T_{\text{OSL}} (2\text{D Mode})$	$(R_{\text{OG1}} - R_{\text{IG1}})/R_p$	x_s
Φ_2	-	0.64	0.70	0.49
Φ_4	-	1.09	1.19	0.73

6.4 2D results using traditional smoothed potentials

In this subsection, we consider how well the second, Φ_2 , and fourth order, Φ_4 , smoothed potentials, using a range of smoothing lengths, are able to match the physics of 3D simulations. Müller et al. (2012) performed this analysis in a form restricted to the shape of torque excitation and the second order potential only. In addition to showing $\Phi_2, b = 0.7$, in the previous section (Figure 8) we now, in Figure 12, visually compare radial metrics from 2D simulations using potentials $\Phi_2, b = 0.4$; $\Phi_2, b = 0.6$; $\Phi_4, b = 0.7$, and $\Phi_4, b = 1.1$ with 3D simulations. All of these 2D potentials have similar qualitative features, however $\Phi_2, b = 0.4$ and $\Phi_4, b = 0.7$ simulations, dramatically overestimate both torque excitation and gap growth. Of the simulations shown, Φ_2 with $b = 0.6$ approximates 3D results the

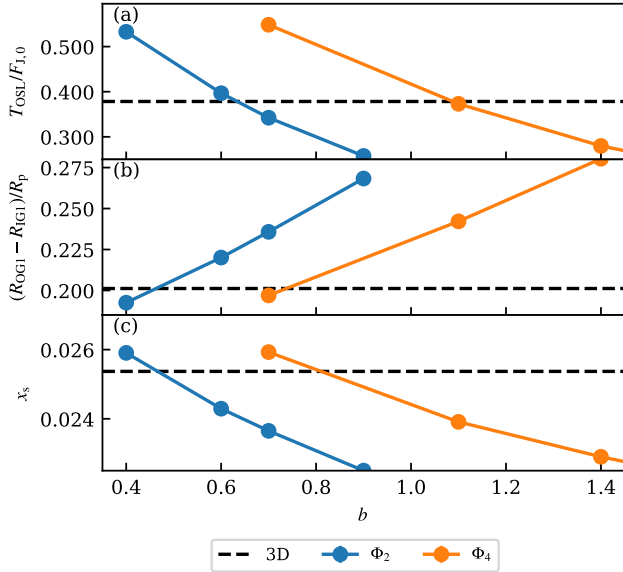


Figure 13. Summary metrics from 2D simulations using second, Φ_2 , or fourth, Φ_4 , order potentials as a function of normalised smoothing length, $b = r_s/H$ (solid lines), compared to results from 3D simulations (dashed black line). As none of these three metrics had a systemic dependence on p or q the values presented here have been averaged across simulations with different background gradients p and q .

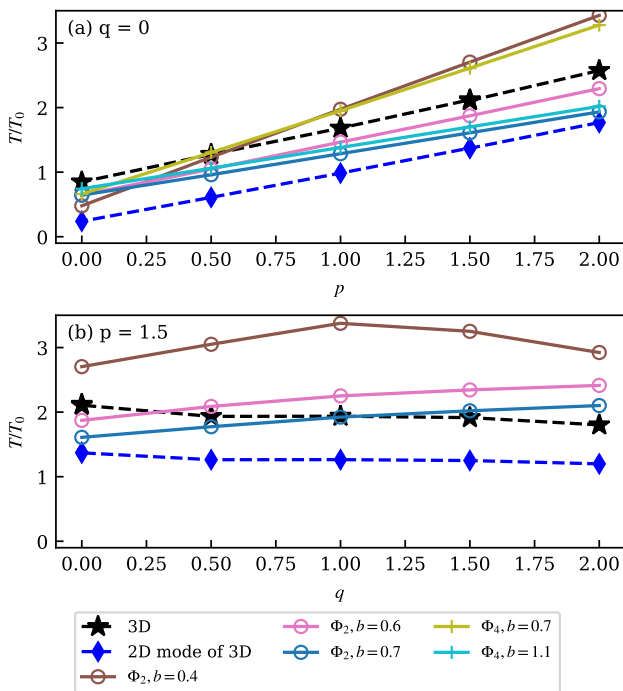


Figure 14. Migration torques as in Figure 11, but with 2D simulations that use the more traditional second, Φ_2 , or fourth, Φ_4 , order smoothed potentials compared with 3D simulations. The fourth order potential, Φ_4 , was only used in globally isothermal simulations and as such has not been included in the lower panel.

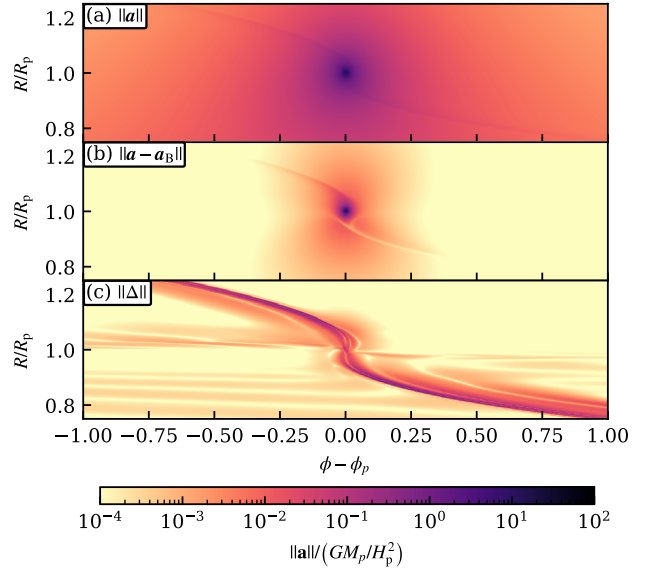


Figure 15. A comparison between the magnitude of 3D gravitational acceleration (a), the magnitude of the difference between actual 3D acceleration and acceleration calculated assuming that the vertical density profile doesn't change from the initial state, i.e. the ‘2D’ gravitational acceleration (Equations 22 and 23) using Σ as calculated from the 3D simulation, (b), and the remainder acceleration term (Equation 12) which describes the acceleration of the ‘2D’ fluid velocities caused by inherently 3D motions (c). These have all been computed from the $p = 1.5$, $q = 0$ fiducial simulation.

best, although those simulations still shows differences from 3D in gap spacings and depth.

In Figure 13, we show how summary metrics differ as a function of smoothing length for Φ_2 and Φ_4 . Summary metrics, other than the migration torque, are independent of p and q . T_{0SL} and x_s both decrease with smoothing length, whereas gap spacing increases with smoothing length. We interpolate these values against our 3D measures to identify the optimal smoothing length for each metric. These are listed in Table 6.4. We find that optimal smoothing lengths are significantly dependent on the metric of choice. Gap spacing and T_{0SL} prefer significantly different smoothing lengths, which is concerning given that these are the physical values that are most likely to directly impact observations (T_{0SL} determines steady state gap depths, e.g. Kanagawa et al. 2015).

In Figure 14, we plot migration torques as a function of smoothing length and background gradient. Generally, migration torques increase with decreasing smoothing lengths, but as the gradients of the torques also change there is no single smoothing length that can match the torque structure of the 3D simulations. This confirms expectations from linear theory (Tanaka & Okada 2024).

7 DISCUSSION

In the previous section we showed that there are some fundamental differences between 2D and 3D simulations of planet–disc interactions, but that 2D simulations are still able to provide good predictions for gap profiles. From these analyses we suggest that Φ_{B,H_p} is the optimal way to treat the planetary potential in 2D simulations – as even though Φ_B may be more theoretically justified, Φ_{B,H_p} provides a more accurate torque approximation. We find, generally however,

Table 3. Average proportional systematic errors associated with 2D simulations that use different forms of the planetary potential as compared to our 3D simulations. This is defined as $\frac{y_{2D}(p,q) - y_{3D}(p,q)}{y_{3D}(p,q)}$ for some value y , which is then averaged over all values of p and q where 2D simulations exist. We use this definition rather than the RMS error to retain the systematic direction of the error.

	$\frac{\Delta T}{T_{3D}}$	$\frac{\Delta T_{OSL}}{T_{OSL,3D}}$	$\frac{\Delta(R_{OG1} - R_{IG1})}{R_{OG1,3D} - R_{IG1,3D}}$	$\frac{\Delta x_s}{x_{s,3D}}$
Φ_B	-0.34	-0.11	0.08	-0.04
Φ_{B,H_p}	-0.05	-0.10	0.07	-0.04
$\Phi_2, b = 0.4$	0.22	0.41	-0.04	0.03
$\Phi_2, b = 0.6$	0.06	0.05	0.10	-0.04
$\Phi_2, b = 0.7$	-0.02	-0.10	0.18	-0.06
$\Phi_4, b = 0.7$	0.26	0.45	-0.01	0.02
$\Phi_4, b = 1.1$	-0.12	-0.01	0.22	-0.06

that 2D simulations are not capable of capturing all of the physical ingredients leading to the migration torque, and do not reproduce horseshoe vortensity striping.

To understand the origin of these differences, we should go back to Section 2 and the discussion after equation (16), where we identified two key factors making 2D and 3D fluid equations different in isothermal discs: the Δ term given by equation (12) and the deviation of the modelled planetary acceleration (e.g. \mathbf{a}_B given by equations (22), (23) if one assumes that the vertical density distribution is unchanged) from the true vertically-integrated 3D acceleration \mathbf{a} , see equation (14). In Figure 15, we plot in panel (b) the magnitude of the difference between \mathbf{a} and \mathbf{a}_B obtained from either the density of a 3D simulation or the surface density of that same simulation, to be compared with $\|\mathbf{a}\|$ itself, shown in panel (a); both are normalized by GM_p/H_p^2 , a characteristic acceleration at the distance of H_p from the planet. The deviation from \mathbf{a} is most important within one H_p of the planet where the hydrostatic envelope forms driving deviations of ρ from ρ_0 (assumed in computing \mathbf{a}_B). Outside this region the differences are small, meaning that there \mathbf{a}_B approximates \mathbf{a} quite well. We also show a map of $|\Delta|$ in panel (c), which demonstrates that the remainder term is significant mainly around the planet-driven density wake (and also likely contributes to horseshoe vortensity striping). The non-trivial contributions provided by these two factors in different parts of the disc are what ultimately precludes the exact correspondence between the results of 2D and 3D simulations.

It is possible to create a ‘more correct’ form of \mathbf{a} by including some of the effects of the planet on the vertical density distribution. Müller et al. (2012) attempted this by estimating an adjusted scale height in the vicinity of the planet. However, while this is possible, across the majority of the disc the deviations due to Δ are of a similar order of magnitude as the deviations due to mismatches in gravitational acceleration, and as such adding additional complexity to \mathbf{a} would not necessarily make the convergence between 2 and 3D simulations significantly better.

7.1 Interpretation of observations

To understand how using 2D simulations may affect the interpretation of planet-disc observations, we present the proportional systematic error for our various metrics based on comparison between 2D and 3D simulations in Table 3. While the values presented in the table may not generalise directly with changes in planetary mass and other physical parameters, we believe it can be used as an initial estimate of the systematic bias caused by 2D approximations. For example, simulations using Φ_2 potential with $b = 0.7$, as suggested by Müller et al. (2012), would overestimate gap spacing by 18 per cent (as

shown in Figure 8). If we attempted to connect this to planet mass using a method such as in Dong et al. (2018), who also used Φ_2 potential with $b = 0.7$, we would underestimate the planet mass by a factor of 2.2. Using the same methodology with $\Phi_2, b = 0.6$, another common potential used by e.g. Zhang et al. (2018), Ruzza et al. (2024), Wu et al. (2023), would lead to an underestimate of planet mass of order 30 per cent⁷. Our analysis here is based on gas, rather than dust, dynamics and to fully verify the claim of this paragraph one would need to perform inviscid 3D gas-dust simulations. In addition this error is still smaller than those expected from observational uncertainty alone. Nonetheless, as this error is systematic rather than random, it may in future cause statistically significant biases. For papers that use $\Phi_4, b = 0.7$, (e.g. Cimerman & Rafikov 2021, 2023; Rafikov & Cimerman 2023; Cordwell & Rafikov 2024) the numerical effects are even more significant, and T_{OSL} in those papers would have been underestimated by a factor of two, leading to significant impacts on any estimated timescales.

Unlike Paardekooper et al. (2010, 2011) we find that $b = 0.4$ does not generally provide a good match for migration torques, except when $p = 0.5$ and $q = 0$, in addition it greatly overestimates the one-sided Lindblad torque, indicating that it is not capturing the overall physics of the interaction correctly. In fact, we find that no 2D potential is capable of reproducing the scalings the migration torque has with background disc gradients. While this may not be an issue for the very low M_p case where well developed models for the 3D Type 1 torque exist (D’Angelo & Lubow 2010; Tanaka & Okada 2024), the torque on planets of moderate mass, such as $M_p = 0.25M_{\text{th}}$, differ from linear expectation (Masset et al. 2006) and are not as well established. We find that the standard linear calculation from Tanaka & Okada (2024, see their equation (63)) does not provide a good match to our measured 3D migration torques. However, for the *globally* isothermal case there is an acceptable approximation if the horseshoe – rather than linear co-rotation – torque (equation 71 in Tanaka & Okada 2024) is used. Nonetheless, for discs with a non-zero background gradient in temperature the quoted approximation does not work well likely due to non-linear dynamics. These differences cannot be attributed to gap opening or partial Type II migration, as when we measured the migration torques the depth of the gap was less than one percent of the background surface density.

Based on Tables 3 and 6.4, we suggest that, if the Bessel-type potential is not used, that the second order smoothed potential with $b = 0.64$ is the best alternative. This is very similar to the value of $b = 0.65$ already used as default by the popular code FARGO3D (Benítez-Llambay & Masset 2016). We stress that papers using potentials with non-optimal smoothing will still represent qualitatively correct physics, however the specific numerical values reported by those studies may be different from 3D reality. To study migration torques, there is no specific best fit value of b , as it is highly dependent on p and q . It is not sufficient, either, to choose a value of b based on the initial background indices, as in most cases this choice will lead to inaccurate estimates of T_{OSL} and therefore gap development. As gap depth at any given time can strongly affect the total torque on a planet, this too will lead to inaccurate overall migration.

The differences in total torque between the 2D and 3D cases may also affect long term gap structure. While in the early stages of gap

⁷ We wish to emphasise that this does not discount their important results of Dong et al. (2018), gap spacing/width remains the likely best measure of planetary masses in continuum observations. We use their work as an example as they have provided a formulae from which we can estimate the systematic error, this error will be shared by any other method that uses gap spacing as a key observable.

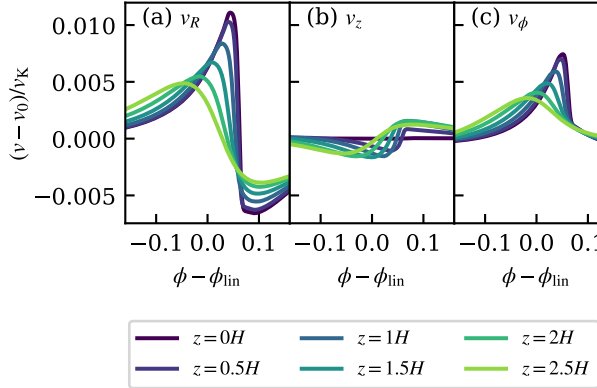


Figure 16. Velocity structure near the shock front at $R = 1.1R_p$, as a function of altitude above the midplane, for our fiducial 3D simulation.

opening the total torque does not have a significant effect on gap structure, at viscous steady state the amplitude of the density pile up exterior to a planetary orbit is determined by the total torque on the planet (Dempsey et al. 2020). Therefore effects that are dependent on the scale of this pile up such as pebble isolation masses (Bitsch et al. 2018), or stalling radii for actively accreting massive planets (Scardoni et al. 2022), may be different in 3D than in existing 2D analysis simply because the total torque is different.

7.2 Implications for velocity kink observations

3D effects also impact the structure of observed velocity kinks (e.g. Disk Dynamics Collaboration et al. 2020). In Figure 5 we showed how the density of the planetary wake changes with altitude, and now in Figure 16 we show how fluid velocity perturbations near the shock front vary with z . One can see that velocity perturbations in R and ϕ show monotonic decrease in amplitude with z , by around a factor of 2 going from the midplane to $z = 2H$, while the deviation in v_z reveals a more complicated behaviour.

There are two key effects in 3D that can change interpretation of velocity kink observations. Firstly, since the magnitude of the velocity signal is smaller one scale height above the disc (where we expect typical velocity tracers, such as the ^{12}CO line, to be emitted) than at the midplane, interpretation of kinematic signatures using 2D simulations may underestimate the underlying planet mass. Secondly, while the magnitude of v_z is smaller than that of v_R or v_ϕ (at one scale height above the mid-plane its magnitude is approximately 20% v_R), it may still be the dominant component of the line of sight velocity deviation for very face-on systems with disc inclinations up to $\sim 10^\circ$. While some existing studies of velocity kinks use fully 3D simulations (e.g. Pinte et al. 2019), others use underlying 2D hydrodynamic models (e.g. Gardner et al. 2025), and analytical studies have often focused on how planet-disc interactions affect v_ϕ only (e.g. Wölfer et al. 2025). We caution that excluding altitude dependence of velocity perturbations and the vertical velocity component may significantly misrepresent the expected signals from velocity kinks, although we leave a thorough investigation of these features to future work.

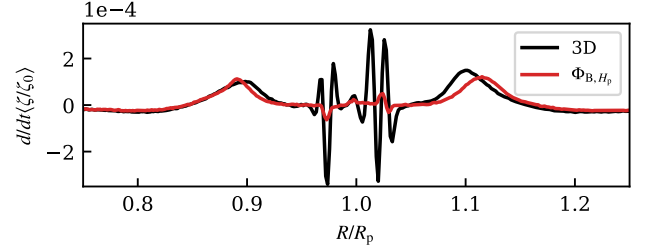


Figure 17. Time derivative of integrated vortensity as measured from a 3D simulation and a 2D simulation using the potential Φ_{B,H_p} between orbits 10 and 11. The additional movement of vortensity in 3D simulations may complicate the dynamical co-rotation torque. The time averaged evolution of vortensity in this region is somewhat smaller than this plot suggests though there is still significant evolution of vortensity in this region for at least the first 100 orbits of the simulation.

7.3 Future Work

A key limitation of this study is the adoption of the locally isothermal equation of state and have ignored radiative effects. The second paper in this series, Ziampras et al. (2025), addresses this concern through a comparison of 2D and 3D simulations with radiation or beta-cooling enabled. We also only tested a single planetary mass in our simulations. While we do not expect the main results to depend on mass – we do not include any explicit dependence on the planetary mass in our smoothed potentials and our recommended potential does not require the fitting of a free parameter – we may see more subtle effects, including different dependencies on the systematic error, at different masses. This is likely to be of highest importance for calculations of migration rates, which even at subthermal masses can deviate significantly from purely linear calculations (e.g. Masset et al. 2006).

In addition, we have not considered how dust dynamics may be affected by 3D effects. As dust often settles closer to the mid-plane the average gravitational force may be larger than for the gas, and it is unclear how this will change 3D circulation. Recently, Rendon Restrepo et al. (2025) derived a Bessel-based formalism to represent 3D gravity in 2D simulations of self-gravitating discs without planets. Their force prescription is equivalent to, though more general than, our α_B definition (equations 23, 22). It remains to be seen if their force prescription will introduce the same types of qualitative error for dust dynamics that we saw for gas in simulations using α_B will occur (see, e.g., Figure 10). Separately for low mass planets, non-axisymmetric dust structures can cause a reversal of migration direction (Benítez-Llambay & Pessah 2018), but this process has only been studied in 2D simulations. This process should be re-analysed in 3D, as we found that there are significant torque differences in 2D versus 3D discs.

While we have not considered migrating planets in this work we advise that the ‘horseshoe vortensity striping’ feature may modify the dynamical co-rotation torque (DCT) (e.g. Paardekooper & Papaloizou 2009). The DCT occurs due to conservation of vortensity within the planet’s horseshoe region, which as the planet migrates through the disc causes a contrast between the vortensity in the horseshoe region and the background vortensity of the disc. However unlike in 2D models, in 3D vortensity is not conserved. In Figure 17, we show the generation of additional vortensity in the horseshoe region due to horseshoe vortensity striping. We checked that this vortensity generation was not merely a transient effect, and

found that while it did start to saturate over a number of libration timescales, that it is possible that it would affect longer term vortensity evolution. We leave in-depth analysis of this vortensity growth and its relationship to the DCT to future work.

Finally, we have not attempted to create semi-analytical formulae for shock formation or angular momentum deposition in 3D discs (such those derived for 2D discs using Φ_4 , $b = 0.7$ in [Cimerman & Rafikov \(2021\)](#)). This is well outside of the scope of this paper, but creating such a model would be useful both for population synthesis models or for the modelling of velocity kinks.

8 SUMMARY

In this paper we investigated the differences between 2D and 3D representations of isothermal planet–disc interactions through a large grid of hydrodynamic simulations, including tests of several different possible representations of the effective planetary gravity in 2D.

- Reduction of 3D fluid equations to 2D is a non-trivial exercise that does not result in direct correspondence between the two limits. Some simplifying assumptions are necessary to justify a 2D approach.
- There is an overall similarity between gap opening in 2D and 3D discs, however in 3D shock formation is altitude dependent. In 3D discs, there is also a significant vortensity evolution in the horseshoe region.
- We find that no 2D simulation using accelerations or potentials explored in this work is capable of correctly reproducing the migration torque caused by a planet across a range of gradients in background surface density and temperature.
- In 2D simulations, we find that the optimal way to represent the planetary potential is with the Bessel-type constant smoothing length potential Φ_{B,H_p} , Equation (24), as initially suggested by [Brown & Ogilvie \(2024\)](#).
- For the standard second and fourth order smoothed potentials, the optimal smoothing length is dependent on the metric of choice. In order to correctly match the one-sided Lindblad torque, the optimal smoothing length for the second order potential is $b = 0.65$, and for the fourth order potential, $b = 1.09$.
- Existing observational analyses of gap profiles may be underestimating the masses of planets carving them by anywhere from ~ 30 to 220 per cent if they rely on standard 2D simulations.
- Interpretation of observations of velocity kinks is likely to be strongly impacted by the 3D structure of the planet-induced perturbation. At low inclinations the vertical velocity component may be the strongest contributor to the signal. For all discs, the vertical dependence of both azimuthal and radial velocity will reduce the observed magnitude of those velocities compare to velocities derived from 2D simulations.

In addition, we developed an interoperable software package, described in Section 5.4, which can extract a large range of important metrics from planet–disc simulations run with different codes. This software package has been made freely available on GitHub: https://github.com/cordwella/disc_planet_analysis.

ACKNOWLEDGEMENTS

A.J.C. is funded by the Royal Society of New Zealand Te Apārangi and the Cambridge Trust through the Cambridge-Rutherford Memorial Scholarship. R.R.R. acknowledges financial support through the

STFC grant ST/T00049X/1 and the IAS. We thank Cristiano Longarini and Samuel Turner for useful discussions, Gennaro D’Angelo and Steve Lubow for their support in the use of their torque model from their 2010 paper, Ruobing Dong for clarifying the smoothed potential used in his 2018 paper, Nicolas Cimerman for an adapted version of ATHENA++ which we further modified for this paper, and Hidekazu Tanaka for useful comments about migration torques.

Software: NUMPY ([Harris et al. 2020](#)), SciPy ([Virtanen et al. 2020](#)), MATPLOTLIB ([Caswell et al. 2023](#)), ATHENA++ ([Stone et al. 2020](#)) and CEPHES ([Moshier 1989](#)).

DATA AVAILABILITY

Simulation data will be made available upon reasonable request to the corresponding author. A version of ATHENA++ with the Bessel-type potentials implemented for planet disc interactions, and the analysis codes developed for this work can be found on GitHub under an open source license to assist future researchers: <https://github.com/cordwella/athena-disk-planet> and https://github.com/cordwella/disc_planet_analysis.

REFERENCES

Andrews S. M., 2020, *Annual Review of Astronomy and Astrophysics*, 58, 483

Balmforth N. J., Korycansky D. G., 2001, *MNRAS*, 326, 833

Benítez-Llambay P., Masset F. S., 2016, *ApJS*, 223, 11

Benítez-Llambay P., Pessah M. E., 2018, *ApJ*, 855, L28

Benítez-Llambay P., Masset F., Koenigsberger G., Szulágyi J., 2015, *Nature*, 520, 63

Bitsch B., Morbidelli A., Johansen A., Lega E., Lambrechts M., Crida A., 2018, *Astronomy & Astrophysics*, 612, A30

Brown J. J., Ogilvie G. I., 2024, *MNRAS*, 534, 39

Caswell T. A., et al., 2023, matplotlib/matplotlib: REL: v3.7.4, doi:10.5281/ZENODO.592536, <https://zenodo.org/doi/10.5281/zenodo.592536>

Chameta R. O., Hasegawa Y., D’Angelo G., 2025, *arXiv e-prints*, p. arXiv:2506.13592

Churilov S. M., Shukhman I. G., 1981, *Astronomicheskij Tsirkulyar*, 1157, 1

Cimerman N. P., Rafikov R. R., 2021, *Monthly Notices of the Royal Astronomical Society*, 508, 2329

Cimerman N. P., Rafikov R. R., 2023, *Monthly Notices of the Royal Astronomical Society*, 519, 208

Cordwell A. J., Rafikov R. R., 2024, *MNRAS*, 534, 1394

Crida A., et al., 2025, *The Open Journal of Astrophysics*, 8, 84

D’Angelo G., Lubow S. H., 2010, *ApJ*, 724, 730

D’Angelo G., Henning T., Kley W., 2002, *A&A*, 385, 647

Dempsey A. M., Lee W.-K., Lithwick Y., 2020, *The Astrophysical Journal*, 891, 108

Disk Dynamics Collaboration et al., 2020, Visualizing the Kinematics of Planet Formation, <http://arxiv.org/abs/2009.04345>

Dong R., Rafikov R. R., Stone J. M., Petrovich C., 2011a, *The Astrophysical Journal*, 741, 56

Dong R., Rafikov R. R., Stone J. M., 2011b, *ApJ*, 741, 57

Dong R., Zhu Z., Rafikov R. R., Stone J. M., 2015, *The Astrophysical Journal*, 809, L5

Dong R., Li S., Chiang E., Li H., 2017, *ApJ*, 843, 127

Dong R., Li S., Chiang E., Li H., 2018, *The Astrophysical Journal*, 866, 110

Fridman A. M., Khoruzhii O. V., 1996, *Astrophysics*, 39, 252

Fung J., Chiang E., 2016, *The Astrophysical Journal*, 832, 105

Fung J., Artymowicz P., Wu Y., 2015, *ApJ*, 811, 101

Gardner C. H., et al., 2025, *ApJ*, 984, L16

Goldreich P., Tremaine S., 1979, *The Astrophysical Journal*, 233, 857

Goldreich P., Tremaine S., 1980, *The Astrophysical Journal*, 241, 425

Goldreich P., Goodman J., Narayan R., 1986, *MNRAS*, **221**, 339
 Goodman J., Rafikov R. R., 2001, *The Astrophysical Journal*, **552**, 793
 Harris C. R., et al., 2020, *Nature*, **585**, 357
 Hunter C., 1972, *Annual Review of Fluid Mechanics*, **4**, 219
 Kanagawa K. D., Tanaka H., Muto T., Tanigawa T., Takeuchi T., 2015, *Monthly Notices of the Royal Astronomical Society*, **448**, 994
 Kley W., 1999, *MNRAS*, **303**, 696
 Lega E., Crida A., Bitsch B., Morbidelli A., 2014, *MNRAS*, **440**, 683
 Li H., Li S., Koller J., Wendroff B. B., Liska R., Orban C. M., Liang E. P. T., Lin D. N. C., 2005, *ApJ*, **624**, 1003
 Masset F. S., 2002, *A&A*, **387**, 605
 Masset F. S., Benítez-Llambay P., 2016, *ApJ*, **817**, 19
 Masset F. S., Papaloizou J. C. B., 2003, *ApJ*, **588**, 494
 Masset F. S., D’Angelo G., Kley W., 2006, *ApJ*, **652**, 730
 McNally C. P., Nelson R. P., Paardekooper S.-J., Benítez-Llambay P., Gressel O., 2020, *Monthly Notices of the Royal Astronomical Society*, **493**, 4382
 Miranda R., Rafikov R. R., 2019a, *The Astrophysical Journal*, **875**, 37
 Miranda R., Rafikov R. R., 2019b, *The Astrophysical Journal*, **878**, L9
 Miranda R., Rafikov R. R., 2020, *The Astrophysical Journal*, **892**, 65
 Miyoshi K., Takeuchi T., Tanaka H., Ida S., 1999, *ApJ*, **516**, 451
 Moshier S. L., 1989, Methods and programs for mathematical functions. Ellis Horwood Limited, Chichester, p. 290, <https://www.netlib.org/cephes/index.html>
 Müller T. W. A., Kley W., Meru F., 2012, *A&A*, **541**, A123
 Ostriker E. C., Shu F. H., Adams F. C., 1992, *ApJ*, **399**, 192
 Paardekooper S. J., Papaloizou J. C. B., 2009, *MNRAS*, **394**, 2283
 Paardekooper S. J., Baruteau C., Crida A., Kley W., 2010, *MNRAS*, **401**, 1950
 Paardekooper S. J., Baruteau C., Kley W., 2011, *MNRAS*, **410**, 293
 Paardekooper S.-J., Dong R., Duffell P., Fung J., Masset F. S., Ogilvie G., Tanaka H., 2022, *Planet-Disk Interactions*, doi:10.48550/arXiv.2203.09595, <https://ui.adsabs.harvard.edu/abs/2022arXiv220309595P>
 Pinte C., et al., 2019, *Nature Astronomy*, **3**, 1109
 Pinte C., Teague R., Flaherty K., Hall C., Facchini S., Casassus S., 2023, in Inutsuka S., Aikawa Y., Muto T., Tomida K., Tamura M., eds, *Astronomical Society of the Pacific Conference Series* Vol. 534, *Protostars and Planets VII*. p. 645 (arXiv:2203.09528), doi:10.48550/arXiv.2203.09528
 Rafikov R. R., 2002a, *The Astrophysical Journal*, **569**, 997
 Rafikov R. R., 2002b, *ApJ*, **572**, 566
 Rafikov R. R., Cimerman N. P., 2023, *Monthly Notices of the Royal Astronomical Society*, **519**, 5800
 Rendon Restrepo S., Rometsch T., Ziegler U., Gressel O., 2025, arXiv e-prints, p. arXiv:2506.10812
 Ruzza A., Lodato G., Rosotti G. P., 2024, *Astronomy & Astrophysics*
 Scardoni C. E., Clarke C. J., Rosotti G. P., Booth R. A., Alexander R. D., Ragusa E., 2022, *MNRAS*, **514**, 5478
 Stone J. M., Tomida K., White C. J., Felker K. G., 2020, *The Astrophysical Journal Supplement Series*, **249**, 4
 Takeuchi T., Miyama S. M., 1998, *PASJ*, **50**, 141
 Tanaka H., Okada K., 2024, *ApJ*, **968**, 28
 Tanaka H., Takeuchi T., Ward W. R., 2002, *The Astrophysical Journal*, **565**, 1257
 Teague R., et al., 2025, *ApJ*, **984**, L6
 Virtanen P., et al., 2020, *Nature Methods*, **17**, 261
 Ward W. R., 1991, in *Lunar and Planetary Science Conference*. p. 1463
 Wölfer L., et al., 2025, *ApJ*, **984**, L22
 Wu Y., Baruteau C., Nayakshin S., 2023, *Monthly Notices of the Royal Astronomical Society*, **523**, 4869
 Zhang S., et al., 2018, *The Astrophysical Journal*, **869**, L47
 Zhu Z., Stone J. M., Rafikov R. R., 2012, *ApJ*, **758**, L42
 Zhu Z., Dong R., Stone J. M., Rafikov R. R., 2015, *ApJ*, **813**, 88
 Ziampras A., Nelson R. P., Rafikov R. R., 2023, *Monthly Notices of the Royal Astronomical Society*, p. statd1973
 Ziampras A., Nelson R. P., Paardekooper S.-J., 2024a, Migration of low-mass planets in inviscid disks: the effect of radiation transport on the dynamical corotation torque, <https://arxiv.org/abs/2402.00125>
 Ziampras A., Nelson R. P., Paardekooper S.-J., 2024b, *MNRAS*, **532**, 351

Ziampras A., Cordwell A. J., Rafikov R. R., Nelson R. P., 2025, arXiv e-prints, p. arXiv:2509.20464

APPENDIX A: VERTICAL MODE DECOMPOSITION FOR THE LINEAR PROBLEM

In Section 2, we defined a 2D disc through integration over the vertical structure of a 3D disc. In this section we provide a different approach. Here we use the linearised equations of motion for a 3D disc, which we decompose into vertical modes. The 2D disc is then the part of the disc represented by the lowest order vertical mode. We follow the approach Tanaka et al. (2002) although, as we have no need to solve the final linear equations, we perform only vertical mode decomposition and ignore the azimuthal decomposition into Fourier modes.

We let the background density, pressure and velocity structure of the disc be represented by ρ_0 , p_0 , and \mathbf{v}_0 , where

$$\rho_0(R, \phi, z) = \frac{\Sigma_0(R)}{\sqrt{2\pi}H} \exp\left(-\frac{z^2}{2H^2}\right), \quad (A1)$$

$$\mathbf{v}_0 = (0, R\Omega, 0), \text{ and} \quad (A2)$$

$$\Omega = \Omega_K \left\{ 1 - \frac{1}{2} \left(\frac{H}{R} \right)^2 \left[\frac{3}{2} + p + \frac{q}{2} \left(\frac{z^2}{H^2} + 1 \right) \right] \right\}. \quad (A3)$$

We retain the locally isothermal equation of state and definition of Σ_0 from Equation (19).

The deviation from the background state is written as $p_1 = p - p_0$, $\eta \equiv p_1/\rho_0$, $\eta' = \eta + \Phi_p$ and $\mathbf{u} = \mathbf{v} - \mathbf{v}_0$ (n.b. in this Appendix \mathbf{u} represents a different quantity than in the main text of the paper). Using these definitions the linearized Navier–Stokes equations are

$$\frac{\partial u_R}{\partial t} + \Omega \frac{\partial u_R}{\partial \phi} - 2\Omega u_\phi = -\frac{\partial \eta'}{\partial R} - \frac{q}{R}\eta, \quad (A4)$$

$$\frac{\partial u_\phi}{\partial t} + \Omega \frac{\partial u_\phi}{\partial \phi} + 2Bu_R = -\frac{1}{R} \frac{\partial \eta'}{\partial \phi}, \text{ and} \quad (A5)$$

$$\frac{\partial u_z}{\partial t} + \Omega \frac{\partial u_z}{\partial \phi} = -\frac{\partial \eta'}{\partial z}, \quad (A6)$$

where $B \equiv \Omega + R/2\frac{\partial \Omega}{\partial R}$ is the Oort constant.

We then expand η' and \mathbf{u} into Hermite polynomials, where for any variable x ,

$$x(R, \theta, t, z) = \sum_{n=0}^{\infty} x_n(R, \theta, t) H_n(Z) \text{ with} \quad (A7)$$

$$x_n(R, \theta, t) \equiv \frac{1}{\sqrt{2\pi}n!} \int_{-\infty}^{\infty} e^{-Z^2/2} x(R, \theta, t, HZ) H_n(Z) dz, \quad (A8)$$

where $Z \equiv z/H$ and H_n is the relevant Hermite polynomial defined as in Tanaka et al. (2002). Under these definitions, the surface density deviation, and the z-averaged velocities, are determined solely by the zeroth order vertical mode, i.e. $p_{1,0}, u_{R,0}$, alone.

Writing $H \propto R^\mu$, with $\mu = (3-q)/2$, we insert the Hermite expanded velocity and pressure perturbations to Equations (A4) – (A6). Using the identities and recursions of the Hermite polynomials

from equations 17 and 20 in [Tanaka et al. \(2002\)](#) we find:

$$\frac{\partial u_{R,n}}{\partial t} + \Omega \frac{\partial u_{R,n}}{\partial \phi} - 2\Omega u_{\phi,n} = -\frac{\partial \eta'_n}{\partial R} - \frac{q}{R} \eta_n + \eta'_n n \frac{\mu}{R} + \eta'_{n+2} (n+2) \frac{\mu}{R} (n+1), \quad (\text{A9})$$

$$\frac{\partial u_{\phi,n}}{\partial t} + \Omega \frac{\partial u_{\phi,n}}{\partial \phi} + 2Bu_{R,n} = -\frac{1}{R} \frac{\partial \eta'_n}{\partial \phi}, \text{ and} \quad (\text{A10})$$

$$\frac{\partial u_{z,n}}{\partial t} + \Omega \frac{\partial u_{z,n}}{\partial \phi} = \frac{\partial \eta'_n}{\partial z} + \frac{\eta'_{n+1}}{H} (n+1). \quad (\text{A11})$$

In this step we have chosen to ignore the small z -dependence in the Oort parameter and in Ω . This means we are ignoring some of the couplings between the different vertical modes of u_R , as this will not change the gravitational force terms we can ignore this for simplicity without modifying the results from this section.

The zeroth order, or 2D mode, of the linearized equations are:

$$\frac{\partial u_{R,0}}{\partial t} + \Omega \frac{\partial u_{R,0}}{\partial \phi} - 2\Omega u_{\phi,0} = -\frac{\partial \eta_0}{\partial R} - \frac{q}{R} \eta_0 + 2\eta_2 \frac{\mu}{R} - \frac{\partial \Phi_{p,0}}{\partial R} + 2\Phi_{p,2} \frac{\mu}{R}, \quad (\text{A12})$$

$$\frac{\partial u_{\phi,0}}{\partial t} + \Omega \frac{\partial u_{\phi,0}}{\partial \phi} + 2Bu_{R,0} = -\frac{1}{R} \frac{\partial \eta_0}{\partial \phi} - \frac{1}{R} \frac{\partial \Phi_{p,0}}{\partial \phi}, \text{ and} \quad (\text{A13})$$

$$\frac{\partial u_{z,0}}{\partial t} + \Omega \frac{\partial u_{z,0}}{\partial \phi} = \frac{\eta_1}{H} + \frac{\Phi_{p,1}}{H}. \quad (\text{A14})$$

This selection of the zeroth order mode is formally the global equivalent of the local approach in [Brown & Ogilvie \(2024\)](#). In their local, shearing box, approach all terms proportional to μ , i.e. the coupling to other vertical modes in Equations (A12) and (A13), were removed.

For a disc that is symmetric around the midplane, the odd Hermite modes are uniformly zero. In the case that the initial state of the disc is symmetric and the planet's orbit is not inclined, the odd modes will be zero for all time, and therefore $u_{z,0} = 0$ for all time. Except in the case that $\mu = 0$, which implies an unlikely temperature gradient of $p = 3$, the lowest order mode cannot be decoupled from higher order modes. It is impossible to calculate the lowest order mode accurately without at least including some of the higher order modes. Regardless, we can still calculate the gravitational force on this mode and assume that $\eta_2 = 0$ to get a closed set of equations for $u_{R,0}$ and $u_{\phi,0}$.

Thus, to evaluate the gravitational force on a 2D disc, or somewhat equivalently the lowest order vertical mode of a 3D disc, we need to know $\Phi_{p,0}$, $\Phi_{p,1}$ and $\Phi_{p,2}$. As the planet we consider has no inclination $\Phi_{p,1} = 0$, and the other two are evaluated as follows:

$$\Phi_{p,0} = \frac{-1}{\sqrt{2\pi}H} \int_{-\infty}^{\infty} e^{-z^2/2H^2} \frac{GM_p}{\sqrt{s^2+z^2}} dz = \frac{-GM_p}{\sqrt{2\pi}H} e^y K_0(y), \quad (\text{A15})$$

$$\Phi_{p,2} = \frac{-1}{\sqrt{2\pi}2H} \int_{-\infty}^{\infty} e^{-z^2/2H^2} \frac{GM_p}{\sqrt{s^2+z^2}} \left(\left(\frac{z}{H} \right)^2 - 1 \right) dz = -\frac{\Phi_{p,0}}{2} + \frac{GM_p}{\sqrt{2\pi}4H} s^2 e^y (K_0(y) - K_1(y)). \quad (\text{A16})$$

Where s is the polar distance as defined in Equation (21) and $y \equiv s^2/4H^2$. Equation (A15) is the same as the Bessel potential, Φ_B as defined in Equation (25). The gravitational acceleration in equations

(A12), (A13), i.e. the terms involving $\Phi_{p,0}$ and $\Phi_{p,2}$, are

$$\begin{aligned} \mathbf{a}_{B,\text{lin}} \cdot \hat{\mathbf{R}} &= -\frac{\partial \Phi_{p,0}}{\partial R} + 2\Phi_{p,2} \frac{\mu}{R} \\ &= \frac{-GM_p}{2H^3 \sqrt{2\pi}R} e^y \left(K_0(y) \left(\mu s^2 + 6\mu H^2 - R^2 + RR_p \cos(\phi - \phi_p) \right) \right. \\ &\quad \left. - K_1(y) \left(\mu s^2 - R^2 + RR_p \cos(\phi - \phi_p) \right) \right), \end{aligned} \quad (\text{A17})$$

$$\begin{aligned} \mathbf{a}_{B,\text{lin}} \cdot \hat{\phi} &= -\frac{1}{R} \frac{\partial \Phi_{p,0}}{\partial \phi} \\ &= \frac{GM_p}{\sqrt{2\pi}H} \frac{R - R_p \cos(\phi - \phi_p)}{2H^2} e^y \left(K_0(y) - K_1(y) \right). \end{aligned} \quad (\text{A18})$$

As in the definition of \mathbf{a}_B (Equations 22 and 23), $\mathbf{a}_{B,\text{lin}}$ is a non-conservative acceleration and cannot be represented as the gradient of some potential.

In addition, we are able to use this framework to define the '2D mode' of the applied torque. The torque the planet applies to the disc is in general given by Equation (31), which we are able to expand into Hermite polynomials as follows

$$\frac{\partial T}{\partial R} \equiv -R \oint \int_{-\infty}^{\infty} \rho \frac{\partial \Phi_p}{\partial \phi} dz d\phi \quad (\text{A19})$$

$$= -R \oint \int_{-\infty}^{\infty} \sum_{n=0}^{\infty} \sum_{m=0}^{\infty} \left(\frac{S_0}{\sqrt{2\pi}} e^{-z^2/2} \frac{\eta_n}{c_s^2} H_n(z) \frac{\partial \Phi_{p,m}}{\partial \phi} H_m(z) \right) dz d\phi. \quad (\text{A20})$$

Which using the orthonormality condition for the Hermite polynomials ([Tanaka et al. 2002](#), equation 13) reduces to

$$\frac{\partial T}{\partial R} = -R \Sigma_0 \oint \sum_{n=0}^{\infty} \frac{\eta_n}{c_s^2} n! \frac{\partial \Phi_m}{\partial \phi} d\phi, \quad (\text{A21})$$

and thus, the zeroth order or '2D mode' of the applied torque is

$$\frac{\partial T}{\partial R} \Big|_{2D} \equiv -R \Sigma_0 \oint \frac{\eta_0}{c_s^2} \frac{\partial \Phi_{p,0}}{\partial \phi} d\phi. \quad (\text{A22})$$

Noting that $\Phi_{p,0} = \Phi_B$ (Equations A15 and 25) and using the definition of η , the 2D torque becomes Equation (32) in the main text.

APPENDIX B: NUMERICAL CONVERGENCE

To ensure that simulation dynamics are converged with respect to the numerical grid scale, we performed a set of convergence tests at increasing resolution. The simulations used surface density and temperature background indices of $p = 1.5, q = 0$ for both our 2D and 3D simulations. For 2D, we used $\Phi_2, b = 0.6$ as the planetary potential. We ran these tests from a lowest resolution of $(N_R, N_\phi) = (450, 1800)$, around 14 cells per scale height at the planet, and performed 4 additional tests, each at double the resolution of the previous simulation up to our largest simulation of $(N_R, N_\phi) = (7200, 28800)$, i.e. 230 cells per scale height. For 3D we started at $(N_R, N_\theta, N_\phi) = (450, 39, 1800)$, with adjustments on the radial width in comparison to 2D to ensure they matched in cells per scale height, and performed higher resolution tests at $(N_R, N_\theta, N_\phi) = (900, 78, 1800)$ and $(N_R, N_\theta, N_\phi) =$

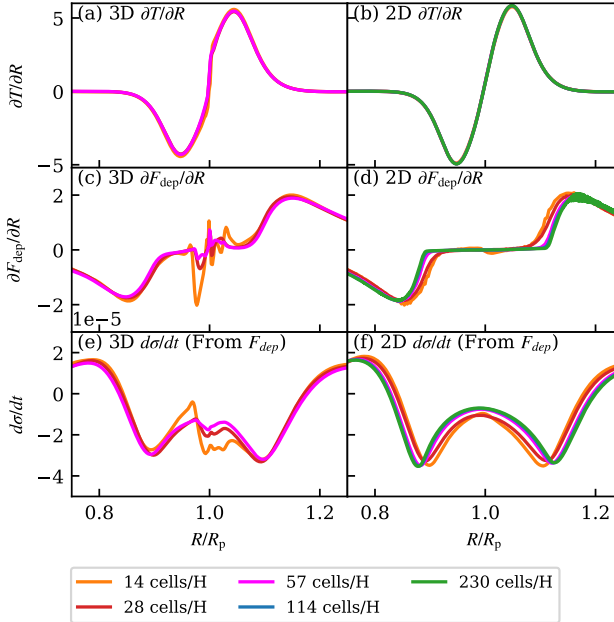


Figure B1. Radial metrics, see Section 5.3.2, from our 2D and 3D grid convergence tests as a function of cells per scale height. The 2D simulations used the second order potential Φ_2 , $b = 0.6$. We use 28 cells per scale height as the fiducial resolution throughout this paper.

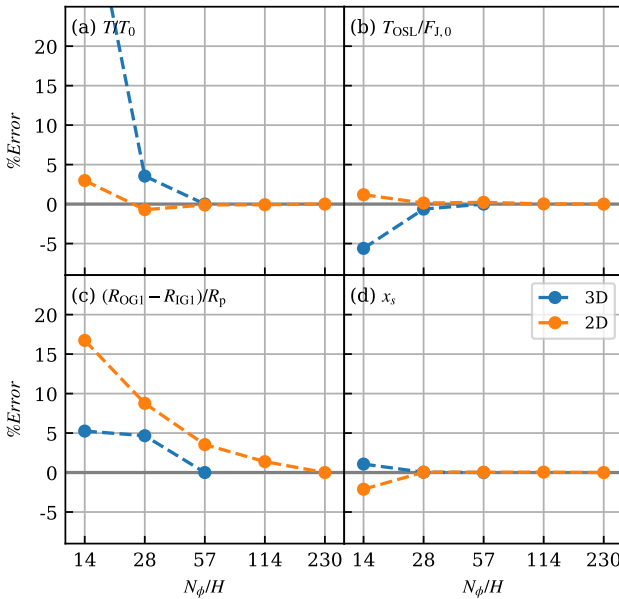


Figure B2. Percentage error in key measures (Section 5.3.3) compared to our highest resolution simulations for 2D and 3D simulations as a function of resolution. One sided torques and horseshoe widths are converged at our fiducial resolution, however gap spacings and, for the 3D simulations, migration torques are not.

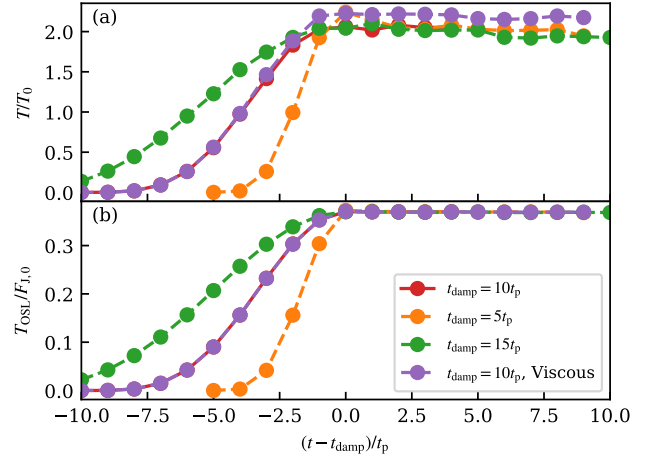


Figure B3. Tests of the temporal convergence of total and one-sided Lindblad torques for simulations with background indices $p = 1.5$ and $q = 0$, as a function of the ramp up time of the planetary potential t_{ramp}

(1800, 156, 7200), i.e. 57 cells per scale height. We processed these simulations using the same process as in the rest of the paper, and show radial and summary metrics in Figure B1 and B2 respectively.

We found that the structure of $\partial T/\partial R$ was converged at our lowest resolution and that the one-sided Lindblad torque and the horseshoe width were converged to a sub-percent level from 28 cells per scale height. In 2D migration torques are well converged at the same resolution. 3D migration torques seem to be converged within 5 per cent of their final value at this resolution, however as we did not test resolutions above 57 cells per scale height in 3D we cannot be sure exactly when this reaches full convergence. We find that gap spacings are still not completely converged at our highest 2D resolution. We find that gap spacing increases with resolution. As resolution increases, the transition in $\partial F_{\text{dep}}/\partial R$ from zero to non-zero values becomes sharper and occurs later - likely due to the a smaller impact of numerical viscosity on the generation of shock structure.

Somewhat disconcertingly, the horseshoe vortensity striping feature (as discussed in Section 6.1.1) shrinks in magnitude with increases in resolution. This can be seen near R_p in Figure B1 (c) and (e). There is no significant effect of resolution on the shape and structure of this feature, but we are unsure what a completely converged version of this structure would look like.

We choose, in this paper, to use a resolution of 28 cells per scale height to run our large grid of simulations. While this does not produce sub-percent numerical convergence for all key values, we find that this marks a good compromise between convergence and computational traceability for a large grid of simulations. This resolution is still significantly higher than many planet-disc interaction simulations.

In Figure B3, we show a plot of temporal convergence for the total and one-sided Lindblad torque for a small selection of our simulations using different ramp up times. We find that the ramp up time for the planetary potential of 10 planetary orbits is sufficient, and that the total torque and one-sided Lindblad torque are both very stable in the first 5 orbits after this point, which is when we typically measure the flow quantities. We also tested a viscous simulation, using $\nu = 2.5 \times 10^{-6}$, with our standard potential ramp up time and

found that the total torque was slightly more stable and slightly larger than in the inviscid case.

APPENDIX C: 1D ANGULAR MOMENTUM EVOLUTION IN A 3D DISK

CR24 derived the 1D (radial) equation for angular momentum evolution starting from 2D disc equations, which enabled them to obtain a number of important results on the early stages of gap opening. Here we extend their approach by obtaining 1D evolution equation starting from 3D fluid equations, which enables us to study gap opening based on the angular momentum deposition profiles extracted from 3D simulations. To do so, we first define the 1D averages, and the deviation from those averages, as follows:

$$\langle \Sigma \rangle(R) \equiv \frac{1}{2\pi} \oint \Sigma d\phi, \quad (C1)$$

$$\langle v_i \rangle(R) \equiv \frac{1}{2\pi \langle \Sigma \rangle} \oint \int \rho v_i dz d\phi, \text{ and} \quad (C2)$$

$$\delta v_i(R, \phi, z) \equiv v_i - \langle v_i \rangle(R), \quad (C3)$$

for $x \in \{R, \phi, z\}$ ⁸.

3D conservation of angular momentum reads:

$$\begin{aligned} R \frac{\partial}{\partial t} (\rho R v_\phi) + \frac{\partial}{\partial R} \left(R^2 \rho v_R v_\phi \right) + R \frac{\partial}{\partial \phi} \left(\rho v_\phi^2 \right) + R^2 \frac{\partial}{\partial z} \left(\rho v_z v_\phi \right) \\ = -R \frac{\partial P}{\partial \phi} - R \rho \frac{\partial \Phi}{\partial \phi}. \end{aligned} \quad (C4)$$

We apply the operator $\frac{1}{2\pi} \oint \dots dz d\phi$ to this equation to find:

$$R \frac{\partial}{\partial t} (R \langle \Sigma \rangle \langle \bar{v}_\phi \rangle) + \frac{\partial}{\partial R} \left(R^2 \langle \Sigma \rangle \langle \bar{v}_\phi \bar{v}_R \rangle \right) = \frac{1}{2\pi} \frac{\partial T}{\partial R}, \quad (C5)$$

where the gravitational torque $\partial T / \partial R$ is defined as in Equation (31).

Using the same transformation as in Equation A9 in CR24 the second LHS term in Equation (C5) becomes

$$\begin{aligned} R^2 \langle \Sigma \rangle \langle \bar{v}_\phi \bar{v}_R \rangle = R^2 \langle \Sigma \rangle \langle \bar{v}_\phi \rangle \langle \bar{v}_R \rangle + \frac{R^2}{2\pi} \oint \int \rho \delta v_\phi \delta v_R dz d\phi \\ = R^2 \langle \Sigma \rangle \langle \bar{v}_\phi \rangle \langle \bar{v}_R \rangle + \frac{1}{2\pi} F_{\text{wave}} \end{aligned} \quad (C6)$$

where F_{wave} is given by Equation (35). Inserting the expanded term, Equation (C6), into Equation (C5) we retrieve the standard 1D angular momentum equation:

$$R \frac{\partial}{\partial t} (\langle \Sigma \rangle R \langle \bar{v}_\phi \rangle) + \frac{\partial}{\partial R} (R^2 \langle \Sigma \rangle \langle \bar{v}_R \rangle \langle \bar{v}_\phi \rangle) = \frac{1}{2\pi} \frac{\partial F_{\text{dep}}}{\partial R}, \quad (C7)$$

with $\partial F_{\text{dep}} / \partial R = \partial T / \partial R - \partial F_{\text{wave}} / \partial R$ as in Equation (33). The 1D equation of mass conservation is the same as in 2D case of CR24. Using this equation, the theoretical surface density evolution formulae from CR24 (see their Appendix C), immediately generalize to 3D.

APPENDIX D: EARLY STAGES OF GAP OPENING FOR DIFFERENT BACKGROUND GRADIENTS

As we have simulated a large grid of 3D planet–disc interaction problems, we are able to use this serendipitously to investigate gap

⁸ It is also possible to derive the 1D angular momentum equations by first averaging the equations vertically, and then averaging those average velocities in azimuth, however this process leads to a more complex form of the 1D equations.

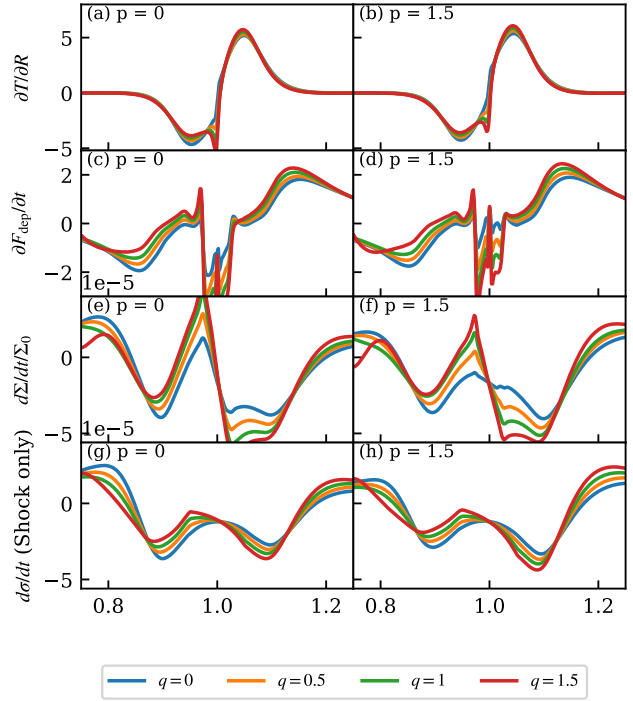


Figure D1. The same radial metrics as in Figure 8, but only showing 3D simulation results and for a larger selection of background temperature gradients. The left-hand column shows simulations with a surface density background index of $p = 0$ and the right-hand column shows those with $p = 1.5$.

formation across a wide range of background surface densities, p , and temperatures, q , thus supplementing the results of CR24. In Figure D1, we show radial metrics for eight of our 3D simulations. We find that neither the spacing between the two gaps nor T_{OSL} differ significantly with p or q , although as q increases the location of each gap shifts to inwards slightly. This may due to more torque being excited in the outer region than the inner as q increases.

CR24 (Appendix C) showed that increasing q , while keeping the same angular momentum deposition profile, lead to slightly shallower inner gaps and slightly deeper outer gaps. However, the effects they measured were very small, almost unnoticeable for $h_p = 0.05$. Therefore the majority of the changes we see in gap structure must be driven by changes in $\partial T / \partial R$ and $\partial F_{\text{dep}} / \partial R$, rather than through changes in how discs at different temperatures respond to angular momentum deposition.

The spikes in $\partial T / \partial R$ near R_p for $p \neq 0$ seem to be related to the horseshoe vortensity striping as discussed in Section 6.1, as these were also seen in the low viscosity simulations of D'Angelo & Lubow (2010), though not in their higher viscosity simulations.